Computers and Geotechnics 150 (2022) 104900

Contents lists available at ScienceDirect

Computers and Geotechnics

journal homepage: www.elsevier.com/locate/compgeo

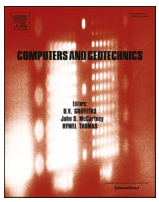

Critical appraisal of pore network models to simulate fluid flow through assemblies of spherical particles

Tokio Morimoto [a,*], Budi Zhao [b], David M.G. Taborda [a], Catherine O'Sullivan [a]

[a] Department of Civil and Environmental Engineering, Imperial College London, London, UK
[b] School of Civil Engineering, University College Dublin, Dublin, Ireland

A B S T R A C T

Coupled numerical models considering fluid flow and particle movement enable fundamental analyses of a variety of phenomena in geomechanics including seepage-induced instabilities. Amongst the various CFD (Computational Fluid Dynamics)-DEM (Discrete Element Method) coupled frameworks which have been proposed, Pore Network Models (PNMs) have the potential to simulate fluid flow in granular materials accurately with a low computational cost to enable simulations on Representative Volume Elements (RVEs). However, the current models of the local conductance between the connected pores are very simple, limiting the accuracy of PNMs. This study develops novel local conductance models by detailed analysis of existing analytical studies of fluid flow through different 3D lattice packings of uniform spheres. The performance of these new models relative to existing, simpler models is demonstrated using CFD simulations in which the flow in the pore space of random assemblies of polydisperse spheres is accurately resolved. The analyses show that the new models proposed here can more accurately predict the local and global permeabilities of specimens with a wide range of void ratios and polydispersities. These models do not require any optimisation via merging pores so that they can efficiently simulate systems with an evolving pore space topology.

1. Introduction

Fundamental understanding of particle-fluid interaction is important in a variety of applications in geomechanics including soil permeability, seepage flow, partially drained shearing, and advective heat transfer. Particle-based hydro-mechanically coupled numerical models that can simulate both fluid flow and particle movement can provide valuable insight into the particle- and pore-scale mechanisms involved in seepage-induced instabilities, liquefaction, and the coupled thermo-mechanical response of fluid-saturated soils. Following Tsuji et al. (1993) and Xu and Yu (1997) (detailed reviews of the available literature can be found in Zhu et al. (2008) and Zhou et al. (2010)), a number of recent studies in geomechanics (e.g. El Shamy and Zeghal (2007)) have used unresolved CFD-DEM (i.e. models that couple computational fluid dynamics and the discrete element method (DEM; Cundall and Strack, 1979)). Where unresolved CFD-DEM is used, an empirical drag expression is required (e.g. Ergun, 1952; Di Felice, 1994). The accuracy of these drag expressions is limited in the case of polydisperse systems (Knight et al., 2020). While it is possible to adapt these methods to account for sub-grid scale variations in porosity (Che et al., 2021), the grid sizes used to simulate the fluid phase are measurably larger than the particles and so local heterogeneities in fluid flow are not captured. Fully resolved CFD-DEM simulations, that discretize the pore space and use a mesh or grid resolution that is smaller than the particles are possible in principle, e.g. using the lattice Boltzmann method (Feng et al., 2007) or the immersed boundary method (Uhlmann, 2005; Knight et al., 2020); however, the large computational cost of these simulations limits their practical use. Pore network models (PNMs) (e.g. Bryant and Blunt, 1992; Chareyre et al., 2012; Kress et al., 2012; Wu et al., 2019; Rong et al., 2020) present a viable alternative to CFD-DEM (Catalano et al., 2014; Yang and Juanes, 2018; Wu et al., 2021): they are computationally more efficient than fully resolved CFD-DEM (Chareyre et al., 2012), and, in contrast to unresolved, they can simulate the local flow heterogeneities.

In a PNM, the pore space is segmented into a large number of individual pores and fluid flow between pores is simulated by idealizing the inter-pore connections as cylindrical pipes whose conductances are determined from the pore geometries. Even in the case of spherical particles, the pore space topology is highly complex (Fig. 1(a)) and so idealizing the passage of fluid between each pair of pores as flow in a cylindrical pipe (Fig. 1(b)) represents a significant simplification of the physical reality. The accuracy of PNMs can be assessed by their ability to correctly predict the overall permeability of the medium. However, if we are to use PNMs in fundamental particle-scale research it is also important to confirm their ability to capture the local flow field.

* Corresponding author.
E-mail addresses: t.morimoto@imperial.ac.uk (T. Morimoto), budi.zhao@ucd.ie (B. Zhao), d.taborda@imperial.ac.uk (D.M.G. Taborda), cath.osullivan@imperial.ac.uk (C. O'Sullivan).

https://doi.org/10.1016/j.compgeo.2022.104900
Received 7 February 2022; Received in revised form 12 May 2022; Accepted 2 July 2022
Available online 18 July 2022

Notations

Greek

α	Geometric factor of a pipe [−]
β_{max}	Maximum angle of a throat face [*rad*]
Γ	Conductance multiplied by the pipe length [m^4]
Γ_{ab}	Γ value of throat *ab* [m^4]
Γ_{ab}^{RP}	Γ value of throat *ab* in a regular packing [m^3]
γ_{ab}	Solid surface area of throat *ab* $[m^2]$
Θ_{ab}	Fluid volume of throat *ab* $[m^3]$
θ	Angle between OF flow vector and PNM flow vector [*rad*]
θ_{peak}	Peak θ value [*rad*]
μ	Dynamic viscosity of fluid [$Pa \bullet s$]
ρ	Pearson correlation coefficient [−]
Ω	Solid angle [sr = steradian]

Latin

A_f	Fluid face area [m^2]
A	Cross-sectional area of a sample [m^2]
b	Length of the unit cell of a regular packing [m]
Cu	Coefficient of uniformity [−]
c_d	Drag coefficient [−]
D	Diameter of a particle [m]
d	Particle distance in FCC packing [m]
ds_c	Mesh length [m]
e	Void ratio [−]
e_{global}	Global void ratio [−]
e_{local}	Local void ratio [−]
e_{max}	Maximum void ratio of packed granular materials [−]
e_{min}	Minimum void ratio of packed granular materials [−]
F	Drag force [N]
f_{ij}	Tensor based on θ [−]
G	Intrinsic conductance of a pipe [m^3]
G_{ab}	Intrinsic conductance of throat *ab* [m^3]
g_{ab}	Hydraulic conductance of throat *ab* $[m^3 Pa^{-1} s^{-1}]$
k	Global intrinsic permeability [m^2]
k_{diag}	Diagonal component of intrinsic permeability tensor [m^2]
k_{ij}	Global intrinsic permeability tensor [m^2]
k_{RP}	Analytical global permeability of a regular packing [m^2]
L	Length [m]
l	Length of the unit cell of a regular packing [m]
l_{ab}	Length of throat *ab* [m]
l^{RP}	Length of the throat in a regular packing [m]
M	Number of throats existing in a granular medium [−]
N_p	Number of particles [−]
n	Number of periodic boundaries [−]
n_i	Unit vector indicating throat direction [−]
$P_{\theta \leq \frac{\pi}{4}}$	Population of θ satisfying $\theta \leq \frac{\pi}{4}$ [%]
p_a	Pressure of pore *a* [Pa]
Q_i	Global volumetric flow rate in i direction [$m^3 s^{-1}$]
Q_{ab}	Volumetric flow rate from pore *a* to pore *b* [$m^3 s^{-1}$]
R	Radius of a cylindrical pipe in Hagen-Poiseuille equation [m]
R^2	Coefficient of determination [−]
r	Radius of a sphere [m]
r_{eff}	Effective radius [m]
r_{eq}	Equivalent radius [m]
r_h	Hydraulic radius [m]
r_{ic}	Inscribed circle radius [m]
S_m	Spherical surface area of a sphere segment m [m^2]
U_i	Flow velocity in i direction [$m \bullet s^{-1}$]
V_{ab}	Total volume of throat *ab* [m^3]
V_m	Volume of a sphere segment m [m^3]
x_i	Coordination in Cartesian coordinate system [m]

Chareyre et al. (2012) conducted Finite Volume (FV) simulations of Stokes flow through packed spheres to validate their PNM; they did not quantify the accuracy of the FV model used, the range of void ratios considered is not documented, and no local flow data were provided. Knight et al. (2020) showed that accurate fully-resolved CFD simulations require careful consideration of the mesh resolution and mesh topology. Sufian et al. (2019) successfully validated their PNM using the validated, fully-resolved CFD data provided in Knight (2019). However, the pore-space segmentation approach that underlies Sufian's PNM includes an optimization step to merge the "over-segmented pores" that emerge from the use of Delaunay triangulation. This optimization incurs a computational cost and leads to a complex data structure. This will pose challenges in the case where a coupled PNM-DEM model is used to simulate systems with an evolving pore space topology in a distributed memory high performance computing environment. Rong et al. (2020) proposed a very accurate approach to the solution of this problem, though it relies on a parameter (r_{CFD}) which requires the numerical solution for parallel flow through the throat cross-section, thus having a large computational cost for large systems or systems where there is an evolving pore-space topology. Consequently, an accurate and viable local conductance model has not been developed yet.

This study considers PNMs that are generated following a triangulation-based partitioning of the void space without any optimizing merging step. It specifically focusses on the selection of an appropriate conductance so that the local flow field can be captured accurately. An overview of pore network modelling with a focus on the available conductance models is given in Section 2. Section 3 develops analytical conductance models for regular packings, which highlights the limitation of the existing conductance models and introduces new models with higher accuracy. Section 4 describes the approaches used to run PNM and CFD simulations of flow through random packings of spheres; data from these simulations are used in Section 5 to critically assess the conductance models proposed in Section 3 considering both local flow and global permeability.

2. Pore Network Models (PNMs)

It's challenging to develop an accurate PNM for granular media with varying packing density and particle size distribution. Moreover, while PNMs present computationally attractive option for modelling flow through granular materials, their accuracy is limited by the simplifications made to model the local conductance. To contextualize the contribution made in this paper, Section 2.1 describes the overall PNM simulation process, while Section 2.2 reviews existing local conductance models and proposes some new models.

2.1. Domain discretisation and local flow calculation in PNM

To construct a PNM of a granular packing the pore space must firstly be discretized into individual pores. This study follows Chareyre et al. (2012) and uses a 3D weighted Delaunay triangulation where the particle centroids are the tedrahedra vertices. Each tetrahedron in the resulting tessellation defines an individual pore (Fig 2(a)). The Voronoi diagram is the dual of the Delaunay tessellation and the weighting which is applied to each vertex (here the weights are equal to the square of the particle radii), prevents any Voronoi vertex from lying within a particle.

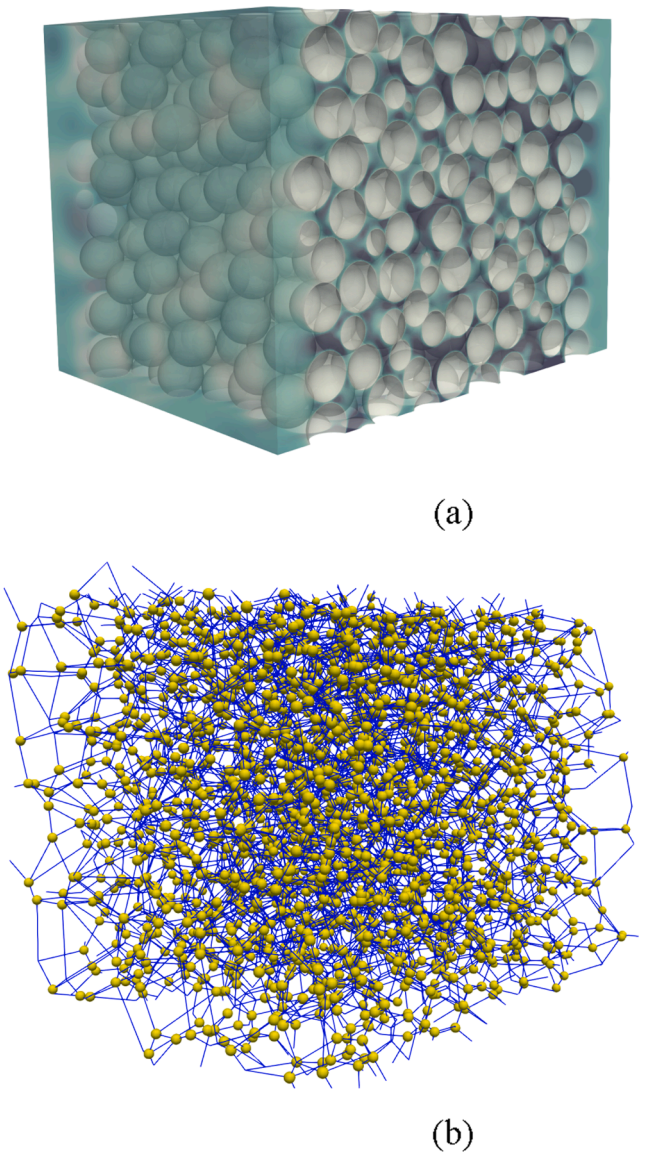

Fig. 1. (a) Complex geometries of the fluid phase in a sphere packing. (b) Complex fluid transport network in the sphere packing (spheres and lines represent pores and edges, respectively).

A schematic illustration of a two-dimensional PNM is shown in Fig. 2 (b). Chareyre et al. (2012) considered the Voronoi vertices to be the nodes in the PNM; this contrasts with many previous studies who took the pore centroids to be the nodes (Sholokhova et al., 2009; Sufian et al., 2019). For each pair of connected pores, Chareyre et al. (2012) defined the pore throat (network edge) to be the domain enclosed by the pore centres and the surfaces of the particles common the two pores (the face particles). In a PNM, the individual pore pressures are defined at the PNM nodes, e.g. p_a in pore a. Flow occurs through the network edges that connect these nodes, e.g. Q_{ab} from pore a to pore b.

To simulate fluid transport between pores, a mass balance equation is considered for each pore assuming steady laminar and incompressible flow:

$$\sum_{i=1}^{4} Q_{ab_i} = 0 \tag{1}$$

where Q_{ab_i} is the volumetric flow rate (in $[m^3 s^{-1}]$) from pore a to pore b_i, and b_i are the (four) pores adjacent to pore a. Assuming laminar flow between any two connecting pores, a and b, Q_{ab} is related to p_a and p_b by application of Darcy's law:

$$Q_{ab} = g_{ab}(p_a - p_b) \tag{2}$$

where g_{ab} is the hydraulic conductance (in $[m^3 Pa^{-1} s^{-1}]$) of the throat connecting pores a and b. While this model can be extended to consider flow characterised by high Reynolds number (Re)(e.g. Wu et al. (2019) and Wu et al. (2021)) by including an inertia term in Eq. (2), the studies presented herein are restricted to low values of Re. The intrinsic conductance of throat ab , i.e., G_{ab} in $[m^3]$, is independent of the fluid dynamic viscosity μ and is given by:

$$G_{ab} = \mu g_{ab} \tag{3}$$

Eq. (1) holds for every pore, and so a system of M linear simultaneous equations (where M is the total number of the pores) must be solved to determine the pressures (p_1, p_2, …, p_M).

Following Eqs. (1) – (3), the G_{ab} values characterising the throats in the system determine the Q_{ab} values of the throats, meaning that accurate modelling of G_{ab} is critical for the performance of the PNM. Calculation of G_{ab} depends only on the geometry of throat ab, as discussed in Section 2.2 below.

2.2. Local intrinsic conductance model in PNM

Most of the existing conductance models that have been documented in the literature are based upon the Hagen-Poiseuille equation, which gives the intrinsic conductance of a pipe as:

$$G = \frac{\alpha \pi R^4}{L} = \frac{\Gamma}{L} \tag{4}$$

with:

$$\Gamma = \alpha \pi R^4 \tag{5}$$

where R is the pipe radius, L is the pipe length, and α is a geometric factor which reflects the pipe shape ($\alpha = 1/8$ for a cylindrical pipe). In a PNM, the distance between the centres of pores a and b (l_{ab}), shown in Fig. 2(b), is taken to be the pipe length L. However, the definitions of R and α are not immediately apparent since the topology of pore throats is complex even in the case of polydisperse spheres. The efficacy of the more widely adopted R and α values, which are outlined below, is considered in this study. A useful analysis of various available expressions for conductance is given in Rong et. al (2020).

2.2.1. Fluid area model (FA model)

This model simply calculates R from the throat face fluid area A_f (defined in Fig. 3(a)):

$$\Gamma = \alpha_{FA} \frac{A_f^2}{\pi} \tag{6}$$

where $\alpha_{FA} = 1/8$, i.e. assuming a circular pipe shape (i.e. a pipe that is circular in cross-section).

2.2.2. Effective radius model (ER model)

Assuming a no-slip boundary condition applies when the fluid is in contact with solid surfaces, the velocity distribution across a throat face depends on the throat face shape (Fig. 3). A throat face completely enclosed by particles, as in Fig. 3(a), has a relatively large low-velocity region. In contrast, the throat face shown in Fig. 3(b) has a large open edge and a higher proportion of the face area transmits relatively fast fluid flow. Bryant and Blunt (1992) defined an effective radius (r_{eff}) as $r_{eff} = \frac{r_{ic}+r_{eq}}{2}$, where $r_{eq} = \sqrt{\frac{A_f}{\pi}}$ and r_{ic} is the radius of the inscribed circle defined by the three particles defining the throat face (illustrated in Fig. 3) so that

$$\Gamma = \alpha_{ER} \pi r_{eff}^4 \tag{7}$$

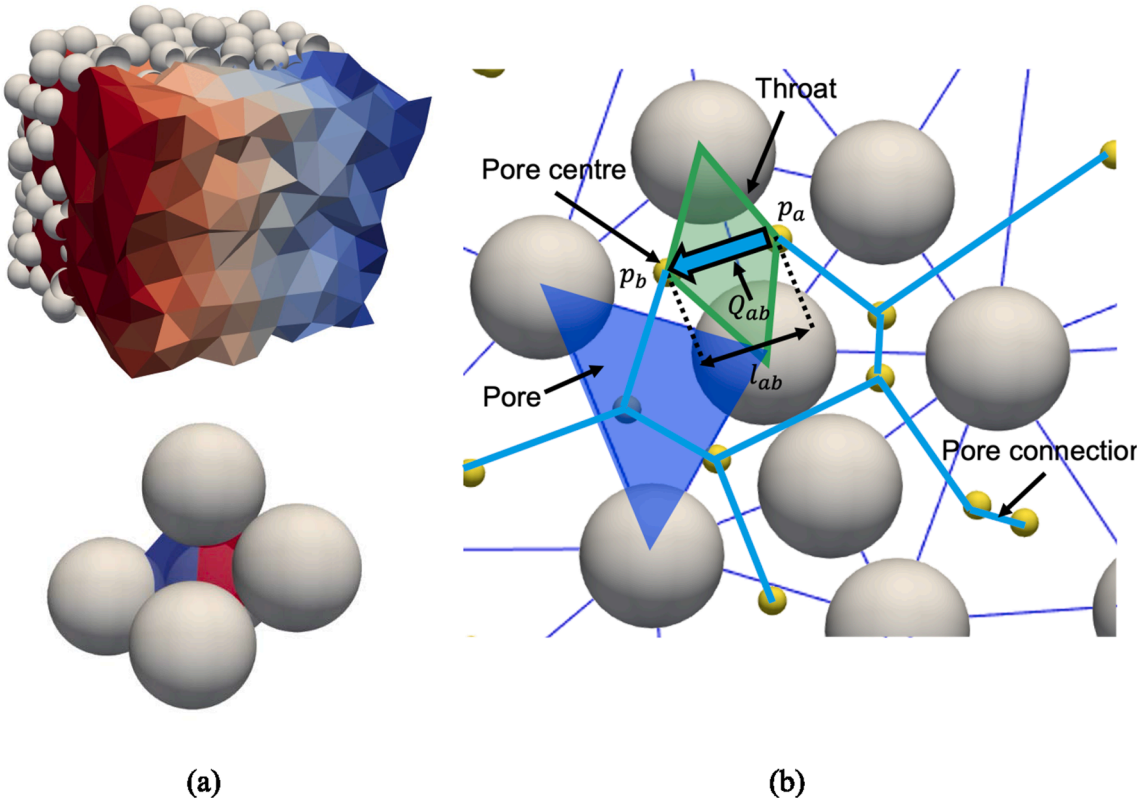

Fig. 2. Schematic illustration of PNM framework. (a) 3D schematic illustrations of fluid domain discretization using the weighted Delaunay triangulation (b) 2D schematic illustration of definition of pores, throats, pore centres and two adjacent pores. The yellow spheres mark the location of the nodes, the turquoise blue lines are the edges of the network, i.e. the pore connections. p_a and p_b are the pressures at pore a and b, respectively, Q_{ab} is the volume flow rate from pore a to pore b and l_{ab} is the length of throat ab.

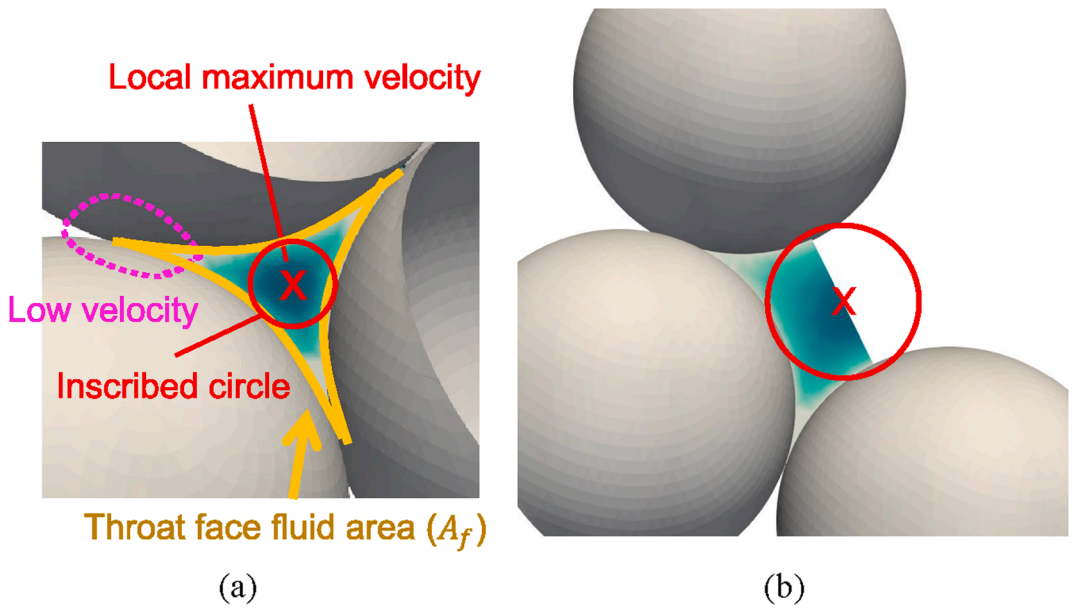

Fig. 3. Schematic illustration of throat face geometries with a definition of an inscribed circle. (a) Closed throat face. (b) Throat face with a large open edge.

where $\alpha_{ER} = 1/8$ for a circular pipe.

2.2.3. Hydraulic radius model (*HR* model)

Chareyre et al. (2012) observed that the *ER* model tends to underpredict the permeability and so they defined the hydraulic radius, r_h, to be the ratio of Θ_{ab} to the solid surface area (γ_{ab}) of throat ab:

$$r_h = \frac{\Theta_{ab}}{\gamma_{ab}} = \frac{\Theta_{ab}}{\sum_{m=1}^{3} S_m} \tag{8}$$

where S_m is the surface area of the part of particle m touching throat ab (illustrated in Fig. 4). Referring to Fig. 4, the volume of throat ab (V_{ab}) is the sum of the volumes of the two tetrahedra defined by pore centres and

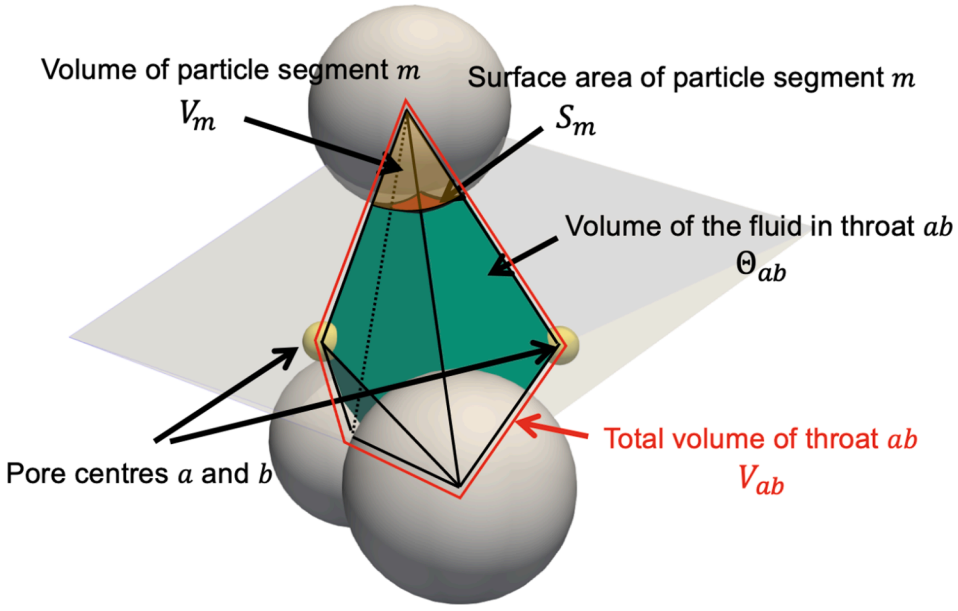

Fig. 4. Schematic illustration of the total volume of throat ab (V_{ab}), the volume of the fluid in throat ab (Θ_{ab}) and the surface area (S_m) and the volume (V_m) of sphere segment$m$

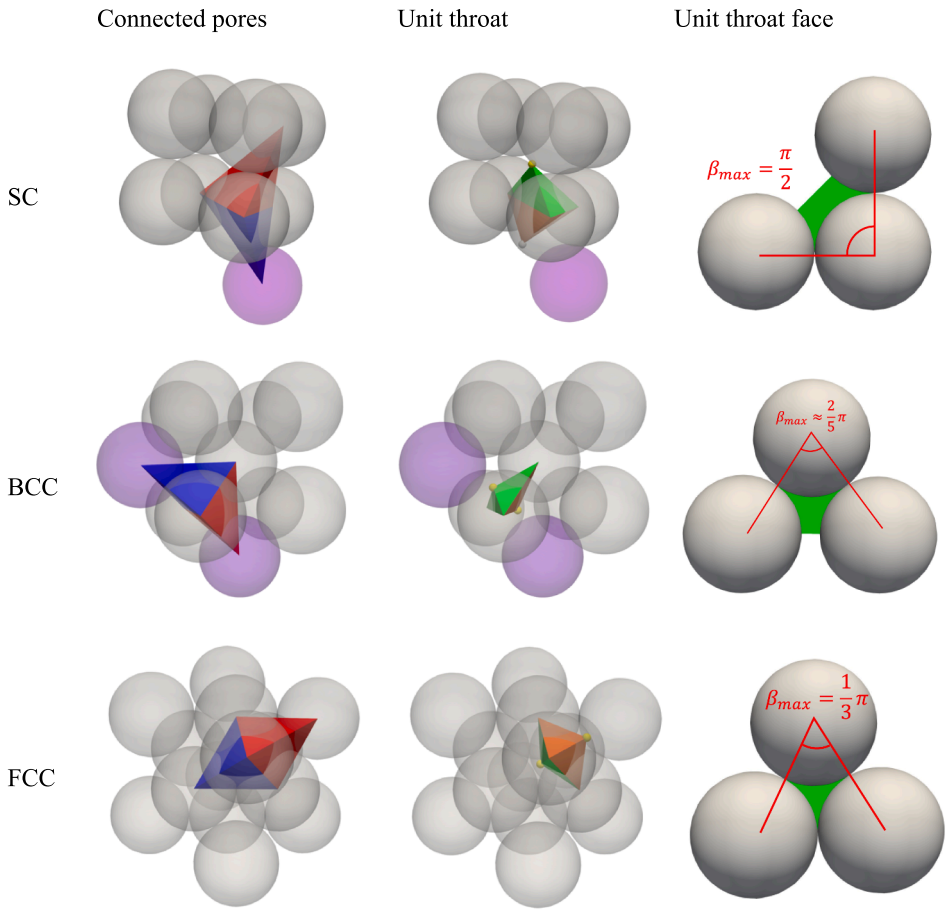

Fig. 5. Schematic illustration of connected pores, unit throats, and unit throat faces in SC, BCC, FCC packings.

the centroids of the face three particles. The volume of the fluid in the throat (Θ_{ab}) is given by subtracting the volumes of the intersection of the face particles with the throat volume from V_{ab}. For a pipe with a circular cross-section,

$$r_h = \frac{\pi R^2 L}{2\pi RL} = \frac{R}{2} \tag{9}$$

Chareyre et al. (2012) suggested using the throat face area A_f and r_h

to calculate Γ:

$$\Gamma = 4\alpha_{HR} A_f r_h^2 \tag{10}$$

While Chareyre et al. (2012) suggest taking $\alpha_{HR} = 1/8$, Sweijen et al. (2018) suggest that the α_{HR} value should be calibrated to capture the global permeability of the particle assembly.

2.2.4. *HR4 model*

The *HR* model includes A_f, which, as shown in Fig. 3, may not effectively characterise the throat geometry. The *HR*4 model, which is introduced in the current study, uses only r_h i.e.:

$$\Gamma = 16\alpha_{HR4}\pi r_h^4 \tag{11}$$

where $\alpha_{ER4} = 1/8$ for a circular pipe.

2.2.5. *ER-HR model*

A new *ER-HR* model, inspired by the models proposed by Bryant and Blunt (1992) and Chareyre et al. (2012) is also considered here, where πr_{eff}^2 is used in lieu of A_f in Eq. (10):

$$\Gamma = 4\alpha_{ER-HR}\pi r_{eff}^2 r_h^2 \tag{12}$$

where $\alpha_{ER-HR} = 1/8$ for a circular pipe.

There are other models, which are not considered here. For example, Patzek and Silin, (2001) and Mason and Morrow (1991) adopted a shape factor defined from the perimeter and the area of a throat face; this shape factor is conceptually similar to the hydraulic radius. We also did not consider the pore-throat-pore model proposed by van der Linden et al. (2018) as it does not perform well without merging Delaunay cells (Sufian et al., 2019). As previously noted (Section 1), Rong et al. (2020) proposed a method to calculate the radius R in Eq. (4) by conducting a CFD simulation of flow through each throat face geometry, following Thompson and Fogler (1997); however, this method is computationally expensive and was therefore not considered in this study. Thompson and Fogler (1997) proposed correcting the conductance of a tube by analytically determining the conductance of a hyperbolic Venturi; this method was not employed here because determining the curvature of the Venturi is challenging in the case of polydisperse granular materials.

3. Analytical study to estimate the Γ and α values of throats in regular packing of uniform spheres

The accuracy of the local conductance model depends on the choice of the radius of the pipe representing the throat (R) and the shape factor α. This section back-analyses data from an analytical study by Zick and Homsy (1982) to estimate the Γ and α values of throats in three regular (lattice) packings of uniform spheres, i.e. simple cubic (SC), body centred cubic (BCC), and face centred cubic (FCC) (Fig. 5). These regular packings enable a constrained study of the conductance models, as only one type of local pore topology exists in each packing. The global permeability data considered are outlined in Section 3.1, and the Γ values are related to these data in Section 3.2. The α values derived from this dataset are then presented in Section 3.3.

3.1. Global permeability of regular packing

Zick and Homsy (1982) used a Galerkin method to study laminar flow around uniform spheres on lattice packings with simple cubic (SC), face-centred-cubic (FCC) and body-centred-cubic (BCC) configurations. They systematically varied the packing density of the systems they considered and provided a set of data in terms of the drag coefficient, c_d, which is given by:

$$c_d = \frac{F}{6\pi\mu r U} \tag{13}$$

where r is the particle radius, U is the inlet velocity, and F is the drag force acting on the particle. These c_d values can be related to the pressure gradient ($\Delta p/L$) across the packing following Zick and Homsy (1982):

$$\frac{\Delta p}{L} = -\frac{9}{2}\frac{\mu}{r^2}\left(\frac{1}{e+1}\right)c_d U \tag{14}$$

Using Darcy's law the analytical global permeability of a regular packing, k_{RP}, can be related to c_d as:

$$k_{RP} = \left|\frac{\mu U}{\frac{\Delta p}{L}}\right| = \frac{2r^2}{9c_d}(e+1) \tag{15}$$

3.2. Back-calculation of Γ

Using the data provided in Zick and Homsy (1982) the intrinsic local conductance between two adjacent pores was estimated from the global permeability data following an approach previously adopted to relate the local thermal conductivity to the global thermal conductivity in heat pipe network models (e.g. El Shamy et al., 2013). The average volume flow rate in the i-direction, $\overline{Q_i}\left[m^3 s^{-1}\right]$ can be expressed as:

$$\overline{Q_i} = \frac{1}{L}\sum_{fp=1}^{M} Q_i^{fp} l^{fp} \tag{16}$$

where L is the length of the system in direction i, M is the number of the pipes in the system, and Q_i^{fp} is the volume flow rate in pipe fp in direction i, and l^{fp} is the length of pipe fp. Following Darcy's law and referring to Eqs. (2)-(4),

$$Q_i^{fp} = -\frac{\Gamma_{ab}^{fp}}{\mu} n_i^{fp}\frac{\partial p}{\partial x_i} = -\frac{\Gamma_{ab}^{fp}}{\mu} n_i^{fp}\frac{\Delta p^{fp}}{l^{fp}} \tag{17}$$

where Γ_{ab}^{fp} is the Γ value of pipe fp connecting pores a and b, n_i^{fp} is the normal unit vector expressing the direction of pipe fp, and Δp^{fp} is the pressure drop through pipe fp. In the case of a lattice system, assuming that the pressure gradient within the system is uniform,

$$\Delta p^{fp} = l^{fp} n_j^{fp}\frac{\partial p}{\partial x_j} \tag{18}$$

where $\frac{\partial p}{\partial x_j}$ is the pressure gradient in direction j.

$$\overline{Q_i} = -\left[\frac{1}{L}\sum\nolimits_{fp=1}^{M}\frac{\Gamma_{ab}^{fp}}{\mu} n_i^{fp} n_j^{fp} l^{fp}\right]\frac{\partial p}{\partial x_j} \tag{19}$$

Dividing by cross-sectional area of the system,

$$U_i = -\left[\frac{1}{V}\sum\nolimits_{fp=1}^{M}\frac{\Gamma_{ab}^{fp}}{\mu} n_i^{fp} n_j^{fp} l^{fp}\right]\frac{\partial p}{\partial x_j} \tag{20}$$

Thus, the intrinsic permeability tensor of the system is:

$$k_{ij} = \frac{1}{V}\sum\nolimits_{fp=1}^{M}\Gamma_{ab}^{fp} n_i^{fp} n_j^{fp} l^{fp} \tag{21}$$

Each lattice configuration has only one type of throat as shown in Fig. 5; thus, each lattice type and packing density has a unique Γ_{ab}^{fp} and l^{fp} value, denoted here as Γ_{ab}^{RP} and l^{RP}. The diagonal terms of the permeability tensor in Eq. (21), $k_{diag}(= k_{xx} = k_{yy} = k_{zz})$, are equal to the analytical global permeability k_{RP} in Eq. (15); therefore,

$$k_{RP} = \Gamma_{ab}^{RP}\frac{l^{RP}}{V}\sum\nolimits_{fp=1}^{M} n_x^{fp} n_x^{fp} \tag{22}$$

Eq. (22) enables back-calculation of the Γ_{ab}^{RP} value from the global permeability k_{RP}. Verification of this approach for deriving analytically

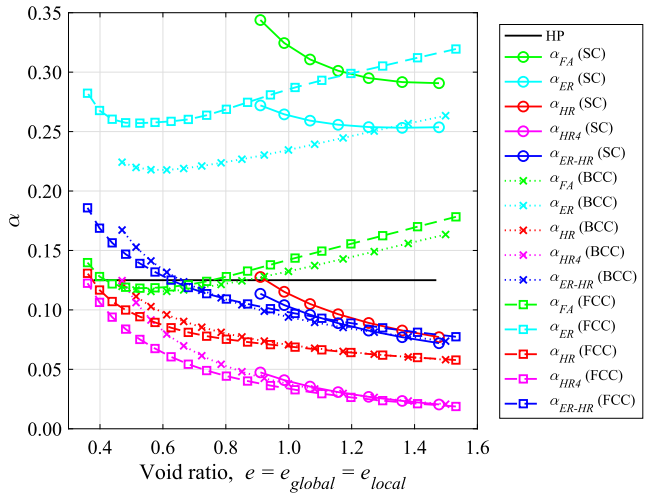

Fig. 6. Analytical study results in terms of α versus e for a variety of models, packings and void ratios. (HP stands for Hagen-Poiseuille's shape factor for flow in a circular pipe = 1/8)

Γ values was carried out using fully resolved CFD data and is documented in Appendix B.

3.2.1. SC packing

The unit cell for the SC packing consists of 6 throats with the same topology. Assuming the lattice is aligned with the Cartesian axes, the unit vector normal to the throat face is $(|n_x|, |n_y|, |n_z|) = (1, 0, 0)$ or $(0, 1, 0)$ or $(0, 0, 1)$, and there are two throats with each unit vector in each unit cell. Denoting the length of the unit cell as b, the volume of the cell is b^3 and the length of the throat l^{RP} is b. Following Eq. (22),

$$k_{RP} = \Gamma^{RP}_{ab}\frac{b}{b^3}(2 \bullet 1 \bullet 1) = \frac{2\Gamma^{RP}_{ab}}{b^2} \tag{23}$$

Taking advantage of the symmetry of the packing, we can calculate the volume of the throat and the sum of the solid angles of the particles within the throat as:

$$V_{throat} = \frac{(Volume\ of\ unit\ cell)}{(Number\ of\ throats)} = \frac{b^3}{6} \tag{24}$$

$$\Omega_{throat} = \frac{4\pi \times (Number\ of\ spheres)}{(Number\ of\ throats)} = \frac{4\pi \times 1}{6} = \frac{2}{3}\pi \tag{25}$$

Note that the solid angle of a sphere is 4π and there is a sphere in the unit cell of the SC packing and so r_h can be calculated once the solid angle within the throat is obtained as:

$$r_h = \frac{(Total\ volume\ of\ the\ throat) - (Solid\ volume)}{(Solid\ surface\ area)} = \frac{V_{throat} - \frac{1}{3}\Omega_{\text{throat}} r^3}{\Omega_{throat} r^2} \tag{26}$$

A_f and r_{eff} can be easily obtained from the face geometry.

3.2.2. BCC packing

The unit cell for the BCC packing consists of 24 throats with the same topology. The unit vector normal to the throat face is $(|n_x|, |n_y|, |n_z|) = (\frac{1}{\sqrt{2}}, \frac{1}{\sqrt{2}}, 0)$ or $(\frac{1}{\sqrt{2}}, 0, \frac{1}{\sqrt{2}})$ or $(0, \frac{1}{\sqrt{2}}, \frac{1}{\sqrt{2}})$, and each of these unit vectors is associated with 8 throats. Just as for the SC packing,

$$k_{RP} = \Gamma^{RP}_{ab}\frac{\frac{\sqrt{2}}{4}b}{b^3}\left(16 \bullet \frac{1}{\sqrt{2}} \bullet \frac{1}{\sqrt{2}}\right) = \frac{2\sqrt{2}\Gamma^{RP}_{ab}}{b^2} \tag{27}$$

$$V_{throat} = \frac{b^3}{24} \tag{28}$$

$$\Omega_{throat} = \frac{4\pi \times 2}{24} = \frac{1}{3}\pi \tag{29}$$

3.2.3. FCC packing

The unit cell of the FCC packing consists of 32 throats with the same topology. The unit vector normal to the throat face is $(|n_x|, |n_y|, |n_z|) = (\frac{1}{\sqrt{3}}, \frac{1}{\sqrt{3}}, \frac{1}{\sqrt{3}})$. Thus,

$$k_{RP} = \Gamma^{RP}_{ab}\frac{\frac{\sqrt{3}}{4}b}{b^3}\left(32 \bullet \frac{1}{\sqrt{3}} \bullet \frac{1}{\sqrt{3}}\right) = \frac{8}{\sqrt{3}}\frac{\Gamma^{RP}_{ab}}{b^2} \tag{30}$$

$$V_{throat} = \frac{b^3}{32} \tag{31}$$

$$\Omega_{throat} = \frac{4\pi \times 4}{32} = \frac{1}{2}\pi \tag{32}$$

3.3. Variation in shape factor α with packing density for lattice packings

Once the Γ values are obtained, the shape factor α defined in Eq. (4) can be determined. For example, the α value for the *FA* model (α_{FA}) is given as:

$$\alpha_{FA} = \frac{\pi\Gamma^{RP}_{ab}}{A_f^2} \tag{33}$$

We calculated α for a range of void ratios, for each of the regular lattice packings considered by Zick and Homsy (1982) (i.e. *SC*, *BCC* and *FCC*), and using the models outlined in Eqs. (6) – (12) (*FA*, *ER*, *HR*, *HR*4 and *ER-HR* models). The minimum void ratios considered for the SC, BCC, and FCC packings were 0.910, 0.470, and 0.361, respectively. In Fig. 6, the calculated α values were plotted against void ratio e; for these packings the local void ratio of the throat (e_{local}) is identical to the void ratio of the packing itself, global void ratio (e_{global}).

Referring to Fig. 6, for the FCC and BCC packings, the back-calculated α_{FA} values are relatively similar over the range of e values considered here (i.e. $0.11 < \alpha_{FA} < 0.18$). However, the α_{FA} values obtained for the SC packing are much larger than those for the FCC and BCC packings. This result shows that the accuracy of any model that uses the throat face fluid area, A_f, depends on both packing type and density. On the other hand, the *ER* model which employs the corrected throat face fluid area seems to be less sensitive to geometrical changes as the α_{ER} values for all the packings are between 0.22 – 0.32. These values are larger than the $\alpha = 1/8$ predicted by the Hagen-Poiseuille equation because the throat cross-sectional area becomes larger towards the end of the throat.

For all the models containing r_h (i.e. *HR*, *HR*4 and *ER* −*HR*), we find that the back-calculated α values decrease as the packing density reduces (i.e. as the void ratio increases); this does not support the use of a constant α as proposed in Chareyre et al. (2012). In models that include A_f term, i.e. the *FA* and *HR* models, there is a large difference between the α values for the SC and BCC packings, i.e. the α values depend upon both fabric and void ratio.

In a lattice packing, the local void ratio of the throat (e_{local}) is identical to the global void ratio (e_{global}). Based upon these analyses of the regular, lattice packings, we introduce an expression that relates the optimal α value for a throat to the void ratio of the throat (denoted as the $\alpha_{XX}(e)$ model, hereinafter, where the subscript XX denotes the model type, i.e. *HR*, *HR*4 or *ER-HR*). The data show that the that α-e relationships for the three lattice packings are almost identical for the *HR*4 and *ER-HR* models. The FCC data are available for a wider range of e values in comparison to the BCC data and so these FCC data were used to develop new cubic equations for α for use with the *HR*, *HR*4 and *ER-HR* models as follows:

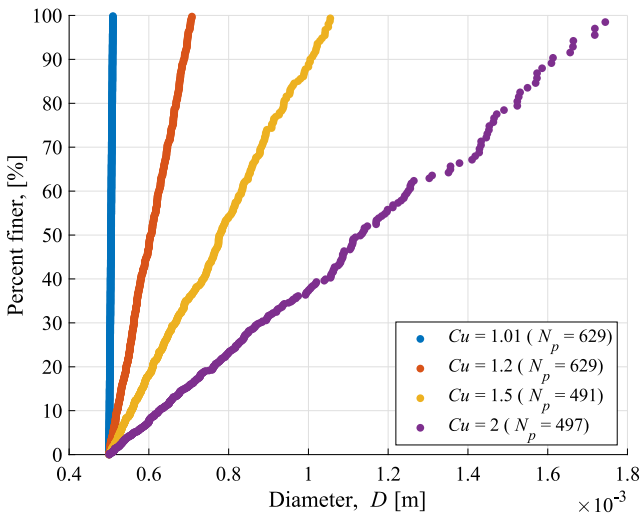

Fig. 7. Particle Size Distributions considered in this study for OF simulations using random packings.

$$\alpha_{HR}(e) = 0.555\left(\frac{1}{1+e}\right)^3 - 0.565\left(\frac{1}{1+e}\right)^2 + 0.279\left(\frac{1}{1+e}\right) \tag{34}$$

$$\alpha_{HR4}(e) = 0.510\left(\frac{1}{1+e}\right)^3 - 0.249\left(\frac{1}{1+e}\right)^2 + 0.062\left(\frac{1}{1+e}\right) \tag{35}$$

$$\alpha_{ER-HR}(e) = 0.510\left(\frac{1}{1+e}\right)^3 - 0.441\left(\frac{1}{1+e}\right)^2 + 0.286\left(\frac{1}{1+e}\right) \tag{36}$$

4. PNM and CFD models to assess applicability of new conductance expressions to randomly packed assemblies of spheres

This section assesses the applicability of the new expressions for α (Eqs. (34)-(36)) in the context of more general packing configurations. The expressions were implemented in a new PNM, as described in Section 4.1. CFD simulations were carried out as outlined in Section 4.2 to back calculate α and enable a direct comparison with the new PNM in terms of global permeability.

4.1. PNM Implementation

The PNM used here was implemented in C++ using appropriate external libraries. The weighted Delaunay triangulation was conducted using TetGen (Si, 2015) following Sufian et al. (2019). The geometric parameters, A_f, r_{eff}, and r_h, are calculated using the positions and radii of the particles. The spherical surface area S_Ω and the volume V_Ω of a sphere segment with a solid angle Ω are calculated using the sphere radius r:

$$S = \Omega r^2 \tag{37}$$

$$V = \frac{1}{3}\Omega r^3 \tag{38}$$

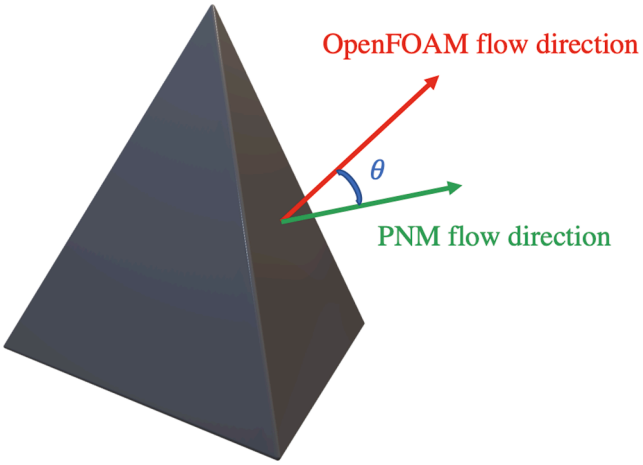

Fig. 9. Schematic illustration on the definition of θ.

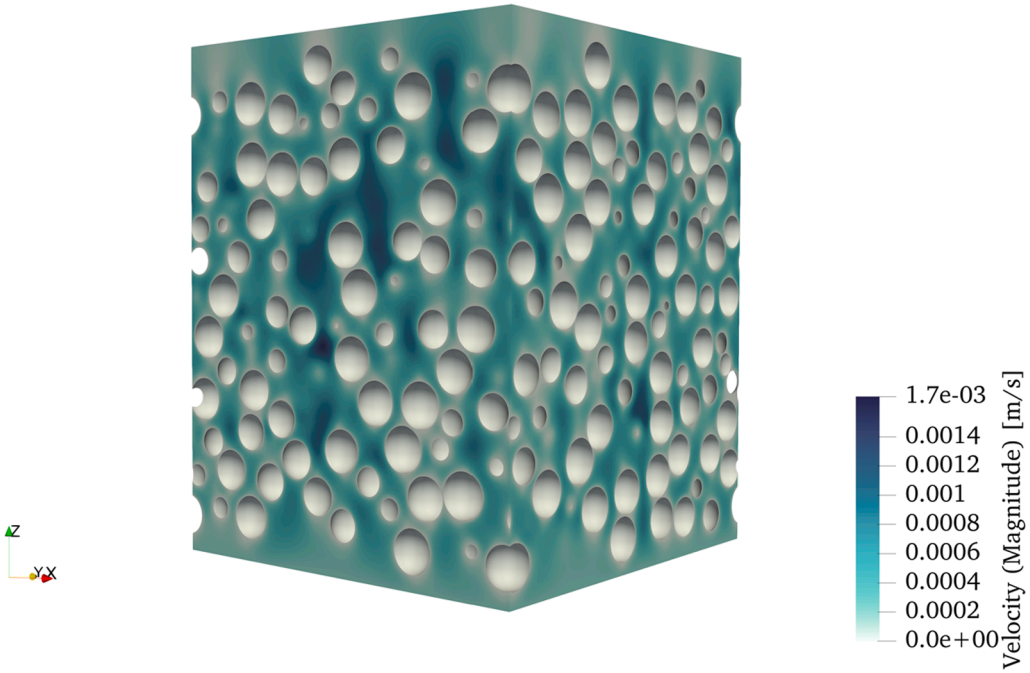

Fig. 8. Geometry of a random packing OF model with a flow velocity field ($Cu = 1.01$, $e = 1.525$)

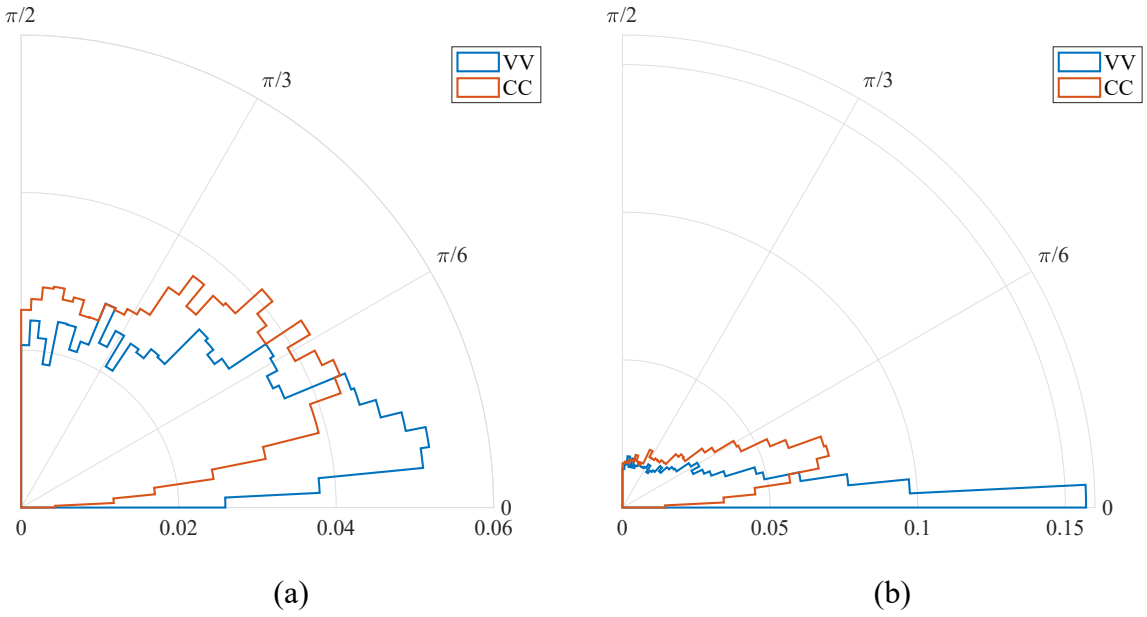

Fig. 10. Distribution of the θ values. (a) $Cu = 1.01$, $e = 1.525$. (b) $Cu = 1.01$, $e = 0.536$.

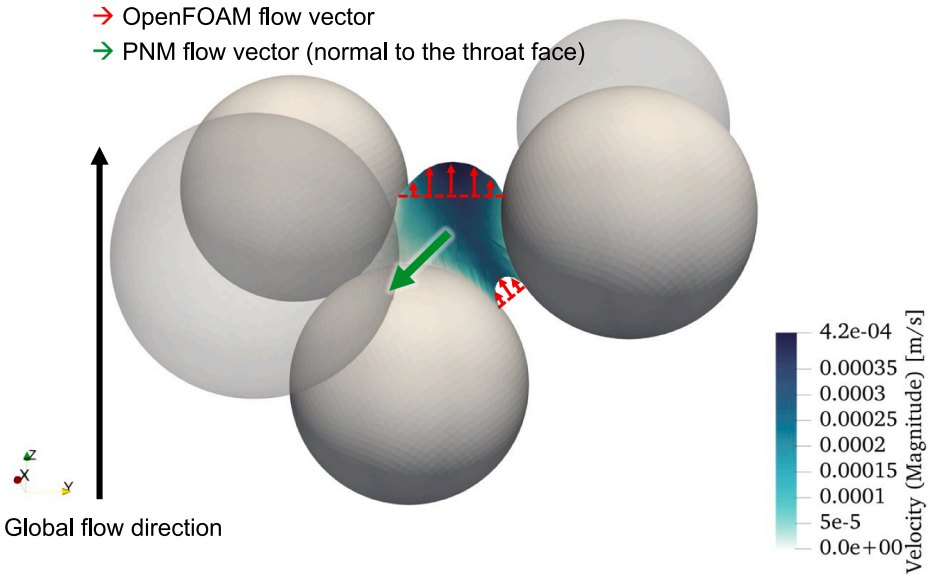

Fig. 11. An example of faces whose flow direction a PNM failed to capture. Face geometry was transformed based on the OF flow vector, which shows that the flow is not normal to the throat face.

where $\Omega = 4\pi$ for a sphere. Following Eq. (8), The hydraulic radius of a throat is then:

$$r_h = \frac{V_{ab} - \sum_{k=1}^{3} V_k}{\sum_{k=1}^{3} S_k} = \frac{V_{ab} - \sum_{k=1}^{3} \frac{1}{3}\Omega_k r_k^3}{\sum_{k=1}^{3} \Omega_k r_k^2} \tag{39}$$

where V_{ab} is the total volume of the throat ab, which can be calculated easily, and S_k and V_k are the spherical surface area and the volume of the segment of particle k which defining the throat (Fig. 4). The algorithm proposed by van Oosterom and Strackee (1983) was used to calculate Ω; this is similar to the implementation in YADE (Šmilauer et al., 2015). The set of M linear equations defined by Eq. (1) were solved using PETSc, a linear equation solver (Balay et al., 1997; Balay et al., 2021). A direct method based on LU decomposition was chosen for robustness since the time for solving the equations is trivial (< 0.1 sec for max. 629 particles).

4.2. PNM simulations

Data for randomly packed spheres generated by Knight et al. (2020) using DEM were used as input for the PNM analyses presented here. Referring to Fig. 7, the selected samples had linear particle size distributions with coefficients of uniformity, Cu , ranging from 1.01 to 2.0 and void ratios e from 0.468 to 1.525, where the void ratio was varied by simulating isotropic compression. The DEM simulations were conducted with periodic boundary conditions along all three cartesian axes directions.

Overall flow in the z-direction was considered, and particles crossing the top maximum (z_{max}) and bottom (z_{min}) boundaries were copied to the opposite z boundary following the procedure adopted by Knight et al. (2020) and Sufian et al. (2019). When partitioning the void space, the two boundaries orthogonal to the z-direction at z_{min} and z_{max} were

Table 1
Tabular summary of distributions of θ values for various packings.

		VV (Voronoi vertex approach)				CC (Cell centroid approach)			
Cu	*e*	θ_{peak} [rad]	θ_{mean} [rad]	SD θ [rad]	$P_{\theta \leq \frac{\pi}{4}}$ [%]	θ_{peak} [rad]	θ_{mean} [rad]	SD θ [rad]	$P_{\theta \leq \frac{\pi}{4}}$ [%]
1.01	1.525	0.15	0.67	0.44	62.5	0.39	0.78	0.41	53.3
	1.174	0.15	0.63	0.44	65.2	0.44	0.74	0.41	57.4
	0.927	0.15	0.60	0.45	67.0	0.29	0.69	0.41	61.9
	0.764	0.05	0.56	0.44	70.0	0.25	0.65	0.41	65.7
	0.610	0.00	0.51	0.45	73.4	0.29	0.61	0.41	69.4
	0.536	0.00	0.48	0.45	75.1	0.25	0.59	0.41	71.3
1.2	1.525	0.10	0.66	0.44	63.2	0.34	0.79	0.41	53.0
	1.174	0.10	0.61	0.44	66.8	0.39	0.75	0.41	56.6
	0.931	0.10	0.58	0.45	68.8	0.39	0.72	0.41	60.4
	0.764	0.00	0.55	0.45	70.7	0.34	0.68	0.41	63.4
	0.613	0.00	0.51	0.46	72.9	0.20	0.63	0.42	67.7
	0.555	0.00	0.49	0.45	74.7	0.25	0.60	0.41	70.5
1.5	1.451	0.10	0.65	0.44	62.8	0.59	0.79	0.40	52.9
	1.174	0.15	0.62	0.45	65.3	0.44	0.76	0.41	56.4
	0.927	0.05	0.59	0.45	68.5	0.44	0.72	0.40	59.8
	0.761	0.05	0.56	0.45	70.7	0.29	0.69	0.41	63.0
	0.610	0.00	0.52	0.46	72.0	0.29	0.63	0.42	66.8
	0.529	0.00	0.48	0.45	74.5	0.20	0.61	0.41	69.5
2.0	1.513	0.20	0.69	0.44	60.1	0.44	0.81	0.41	49.9
	1.227	0.20	0.65	0.45	62.3	0.39	0.79	0.41	52.4
	0.916	0.05	0.61	0.45	66.2	0.29	0.75	0.41	56.6
	0.751	0.05	0.59	0.46	67.6	0.34	0.71	0.42	61.0
	0.603	0.00	0.56	0.46	70.3	0.29	0.67	0.42	64.4
	0.468	0.00	0.48	0.46	74.8	0.25	0.60	0.42	69.8

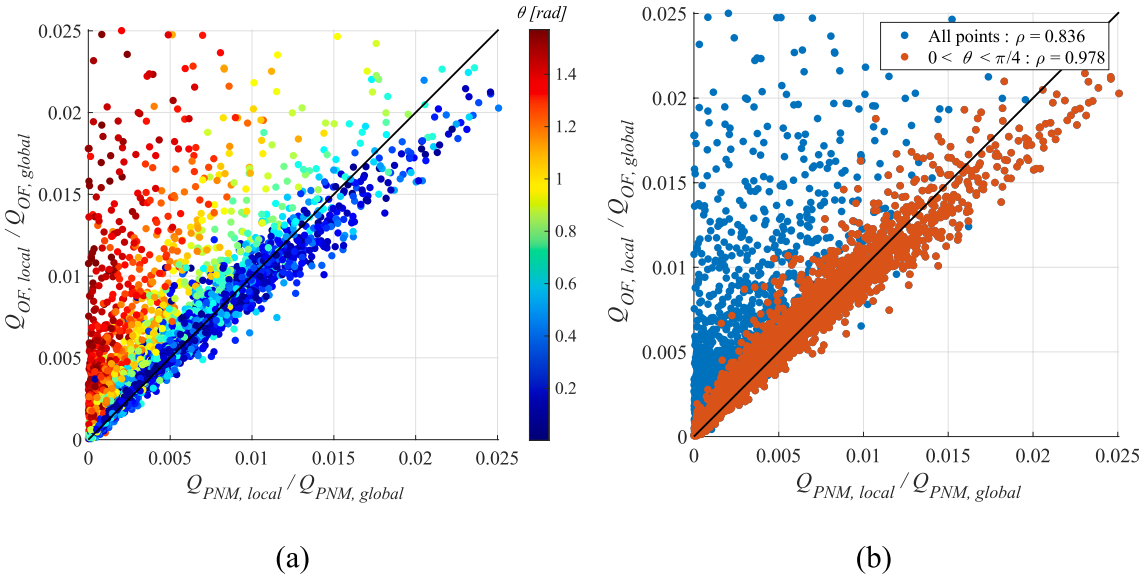

Fig. 12. Comparison of normalized local volume flow rate (in $[m^3 s^{-1}]$) between OF and PNM (HR model with $\alpha_{HR} = 1/8$) for a packing with $Cu = 1.01$ and $e = 0.536$. (a) Coloured by θ values. (b) Markers with $0 < \theta < \pi/4$ are highlighted.

considered to be spheres, with a radius much larger than the sample length along z following Chareyre et al. (2012). For the weighted Delaunay triangulation adopted here, the centre of the pores including these large spheres representing the boundaries then lay approximately on the relevant boundary. Constant pressure boundary conditions were considered with 1 [*Pa*] and 0 [*Pa*] applied at z_{min} and z_{max}, respectively. This constant pressure boundary condition was applied by setting the pressure of the pores including one of the large boundary spheres to the relevant boundary pressure value. In the x- and y- directions, periodic boundaries were used. Details on the implementation of periodic boundaries are provided in Appendix C.

The $\alpha(e)$ models introduced in section 3.3 were implemented in the PNM. Referring to Eq. (38), the e_{local} value of throat ab in a random packing can be calculated using the total volume of the throat ab (V_{ab}), the solid angle Ω_k and the radius r_k of each particle k that defines the throat ab:

$$e_{local} = \frac{Volume\ of\ the\ fluid\ phase\ in\ the\ throat}{Volume\ of\ the\ solid\ phase\ in\ the\ throat} = \frac{V_{ab}}{\sum_{k=1}^{3} \frac{1}{3}\Omega_k r_k^3} - 1 \tag{40}$$

After conducting a flow simulation, the global flow velocity (U) was calculated by summing up the total volumetric flow rate through the z_{min} and z_{max} boundary pores following Chareyre et al. (2012) and Sufian et al. (2019). The intrinsic permeability of the sample (in $[m^2]$) is then:

$$k = \frac{UA}{\mu}\frac{\Delta p}{L} \tag{41}$$

where Δp is the pressure difference applied to the sample, and A and L

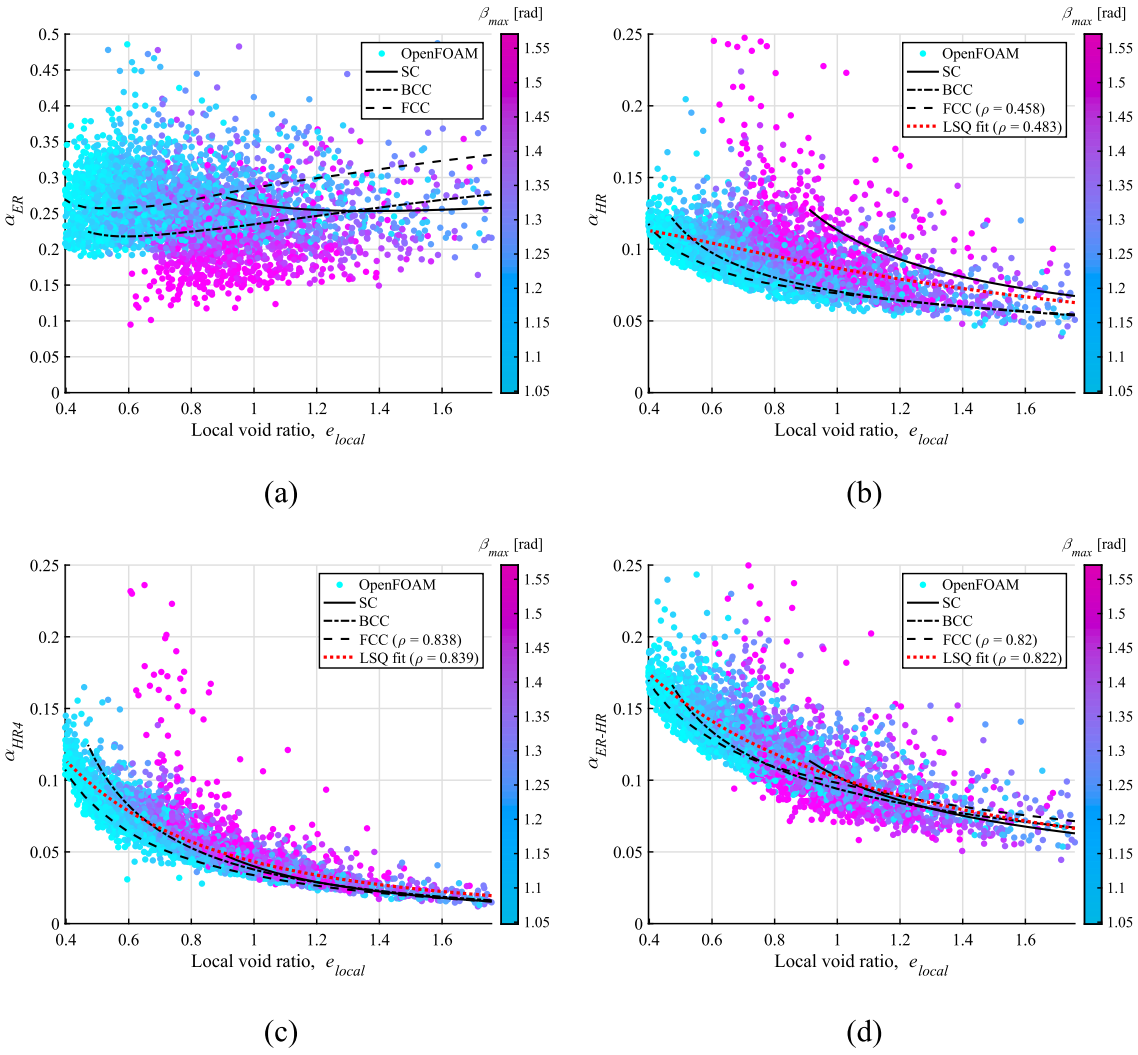

Fig. 13. Comparison of α versus e_{local} between an OF simulation and analytical models for $Cu = 1.01$ and $e = 0.764$. Marker colour gives the maximum angle of the throat face (β_{max}). (a) *ER* model. (b) *HR* model. (c) *HR*4 model. (d) *ER-HR* model.

are the cross-sectional area and the length of the sample, respectively.

4.3. OF simulation using random packings and post-processing

To validate the PNM, rigorously validated fully-resolved CFD simulation data were developed using OpenFOAM with a body-fit mesh generation technique (Knight, 2019; Knight et al. 2020; Knight, 2021). The unstructured mesh generation technique (MeshSpherePacking, MSP) developed by Knight (2019) results in a mesh that fits to the surface of spheres in a cubic space with periodic boundaries. The validation study provided in Appendix A was used to confirm that the adopted simulation approach generated accurate data and to select the coarseness of the mesh. Referring to Fig. A1, based on the validation study, the characteristic mesh length, ds_c, was taken as $d_{min}/30$, where d_{min} is the minimum particle diameter. Hereinafter, we denote a fully-resolved CFD simulation using OpenFOAM as an OF simulation.

The mesh generated by MSP was converted into the polyMesh format, which is a basic mesh format for OpenFOAM. In OpenFOAM SimpleFOAM, an incompressible steady-state solver, was used to solve the continuity and momentum equations (Weller et al., 1998). For all the cases considered here periodic boundary conditions were applied in the $x-$ and $y-$ directions. A constant pressure boundary with a kinematic pressure value of 0 $[m^2s^{-2}]$ was applied at the z_{max} boundary and a constant inlet velocity boundary with a velocity value of $(0, 0, U_z)$ was considered at z_{min} where U_z is the inlet velocity in the $z-$ direction. A no-slip boundary condition was applied at the surface of each particle, i.e. the velocity of the fluid was set to zero at the surface of each particle. The initial velocity field within each mesh element was also set to be $(0, 0, U_z)$ and numerical iterations were conducted until the relative variations in the pressure and the velocity between two successive iterations were $<1 \times 10^{-3}$%. The pressure field and the velocity field were output for post-processing.

The same random packings considered in the PNM (Section 4.2) were used as inputs to MSP for subsequent OpenFOAM simulations. A typical OF model indicating local velocity data is shown in Fig. 8. As in the PNM, any sphere crossing the periodic boundaries at z_{max} or z_{min} boundary was copied to the opposite boundary. After copying the particles, the mesh for the packings was generated using MSP and an OF simulation followed.

The "true" Γ value of the throats in random packings was calculated in the following procedure. The weighted Delaunay triangulation information, namely the IDs of particles defining pores, the Voronoi vertices of pores and pore connections, was output from the PNM. To obtain the "true" Γ value of each throat, the volumetric flow rate vector through the throat face (in $[(m^3s^{-1}, m^3s^{-1}, m^3s^{-1})]$) and the pressure gradient within the throat was interpolated using ParaView (Ahrens et al., 2005). The mesh geometry, flow field, and pressure field were output from OpenFOAM in the vtk format. The mesh on the throat face

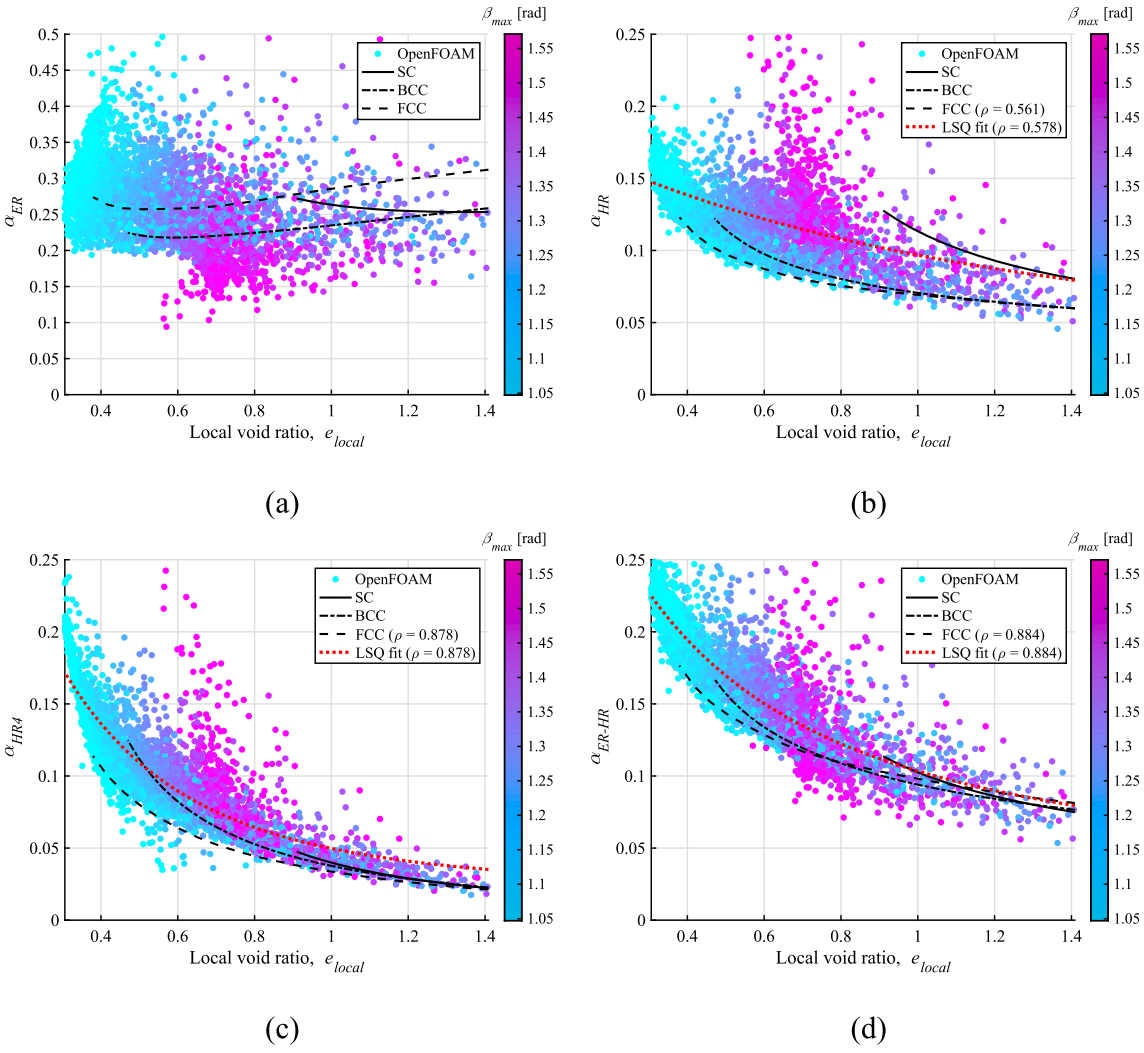

Fig. 14. Comparison of α versus e_{local} between an OF simulation and analytical models for $Cu = 1.01$ and $e = 0.536$. Marker colour gives the maximum angle of the throat face (β_{max}). (a) *ER* model. (b) *HR* model. (c) *HR*4 model. (d) *ER-HR* model.

Table 2
Tabular summary of C_1, C_2 and C_3 values in Eq. (43) for a variety of packings.

		HR			*HR*4			*ER* −*HR*		
Cu	*e*	C_1	C_2	C_3	C_1	C_2	C_3	C_1	C_2	C_3
1.01	0.764	-0.212	0.186	0.134	0.102	0.064	0.146	0.288	-0.010	0.020
	0.61	-0.140	0.102	0.165	0.142	0.051	0.138	0.509	-0.260	0.094
	0.536	-0.097	0.119	0.158	0.412	-0.196	0.202	0.842	-0.596	0.187
1.2	0.764	-0.849	0.869	-0.034	-0.051	0.211	0.114	-0.115	0.415	-0.088
	0.613	-0.626	0.653	0.020	0.033	0.138	0.128	0.165	0.135	-0.016
	0.555	-0.405	0.467	0.062	0.183	0.034	0.146	0.556	-0.269	0.093
1.5	0.761	-0.822	0.838	-0.028	-0.182	0.334	0.081	-0.116	0.414	-0.091
	0.61	-0.520	0.480	0.081	-0.039	0.169	0.130	0.157	0.108	-0.002
	0.529	-0.548	0.624	0.017	0.033	0.185	0.101	0.528	-0.257	0.090
2.0	0.751	-0.423	0.371	0.098	0.035	0.037	0.167	0.057	0.189	-0.030
	0.603	-0.226	0.151	0.162	0.091	-0.029	0.190	0.288	-0.044	0.030
	0.468	-0.172	0.145	0.160	0.164	-0.044	0.182	0.697	-0.490	0.156

was extracted from the vtk file using the **clip** and **slice** functions in ParaView and the total volume flow rate vector through the meshes was interpolated using the **integrateVariables** function. The pressures at pore centres a and b (p_a and p_b) were interpolated using the **ProbeLocation** function. For each pore connection, the volume flow rate vector and the pressures at the centres of the connected pores (p_a and p_b in Eq. (2)) are available. The magnitude of the volume flow rate vector was used for Q_{ab} in Eq. (2) and the "true" Γ_{ab} value was back-calculated, using Eqs. (2) - (4):

$$\Gamma_{ab} = \frac{Q_{ab} l_{ab}}{p_a - p_b} \mu \tag{42}$$

Faces crossing a periodic boundary, which account for at most 20% of the total number of faces, were not considered in the detailed analysis

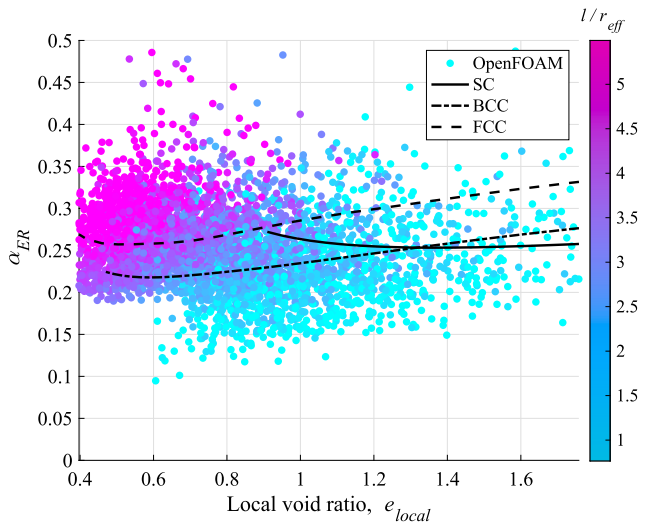

Fig. 15. Comparison of α versus e_{local} between an OF simulation and analytical models for $Cu = 1.01$ and $e = 0.764$. Marker colour gives the normalised throat length (l/r_{eff}).

due to the technical difficulty associated with interpolating the volume flow rate through such faces.

5. Analysis of PNM performance for randomly packed spheres

5.1. Analysis of local flow direction

The direction of flow between a pair of adjacent pores in a PNM is assumed to be parallel to the vector from the centre of a pore to the centre of the other pore. Hitherto the validity of this assumption has not been thoroughly investigated. The pore centre locations determine the flow direction in the PNM, and we considered two definitions here; (1) use of Voronoi vertices following Chareyre et al. (2012) (denoted VV method) and (2) use of the centroids of the pore cells e.g. Sufian et al. (2019) (denoted CC method). Where the VV method is used, the vector is always normal to the throat face.

If the angle between the PNM flow vector and the OF flow vector through a face is θ ($0 \leq \theta \leq \pi/2$) (Fig. 9), the PNM correctly predicts the flow direction at the throat if $\theta = 0$, while $\theta \neq 0$ indicates a discrepancy. The distributions of θ in two random packings ($e = 1.525$ and 0.536 with $Cu = 1.01$) using the VV and CC methods are shown in Fig. 10. For the dilute packing ($e = 1.525$, Fig. 10(a)) neither method correctly captures the flow direction. A typical throat whose flow direction is not accurately predicted by the PNM is shown in Fig. 11. In these cases, the three

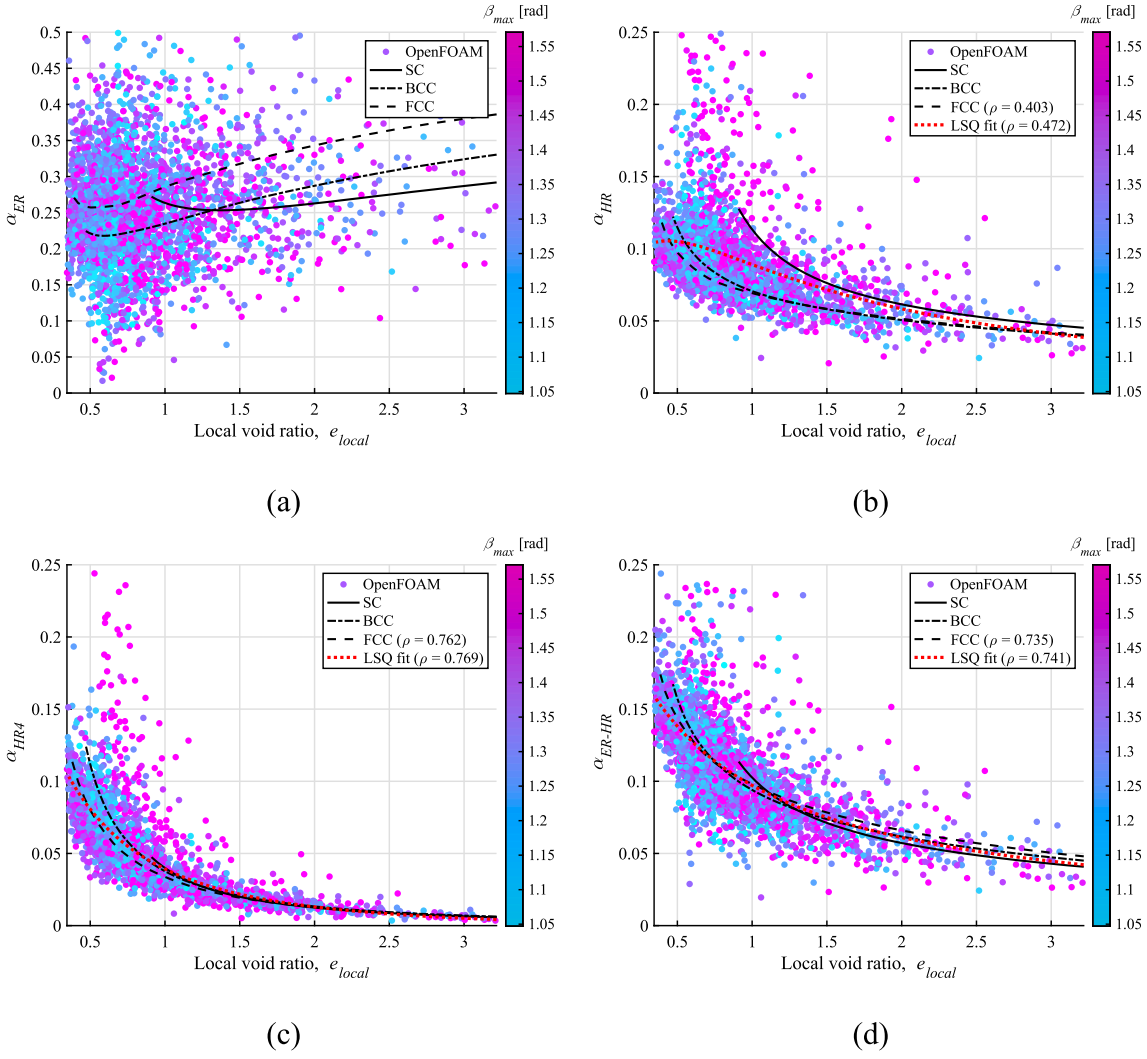

Fig. 16. Comparison of α versus e_{local} between an OF simulation and analytical models for $Cu = 2.0$ and $e = 0.751$. Marker colour gives the maximum angle of the throat face (β_{max}). (a) *ER* model. (b) *HR* model. (c) *HR*4 model. (d) *ER-HR* model.

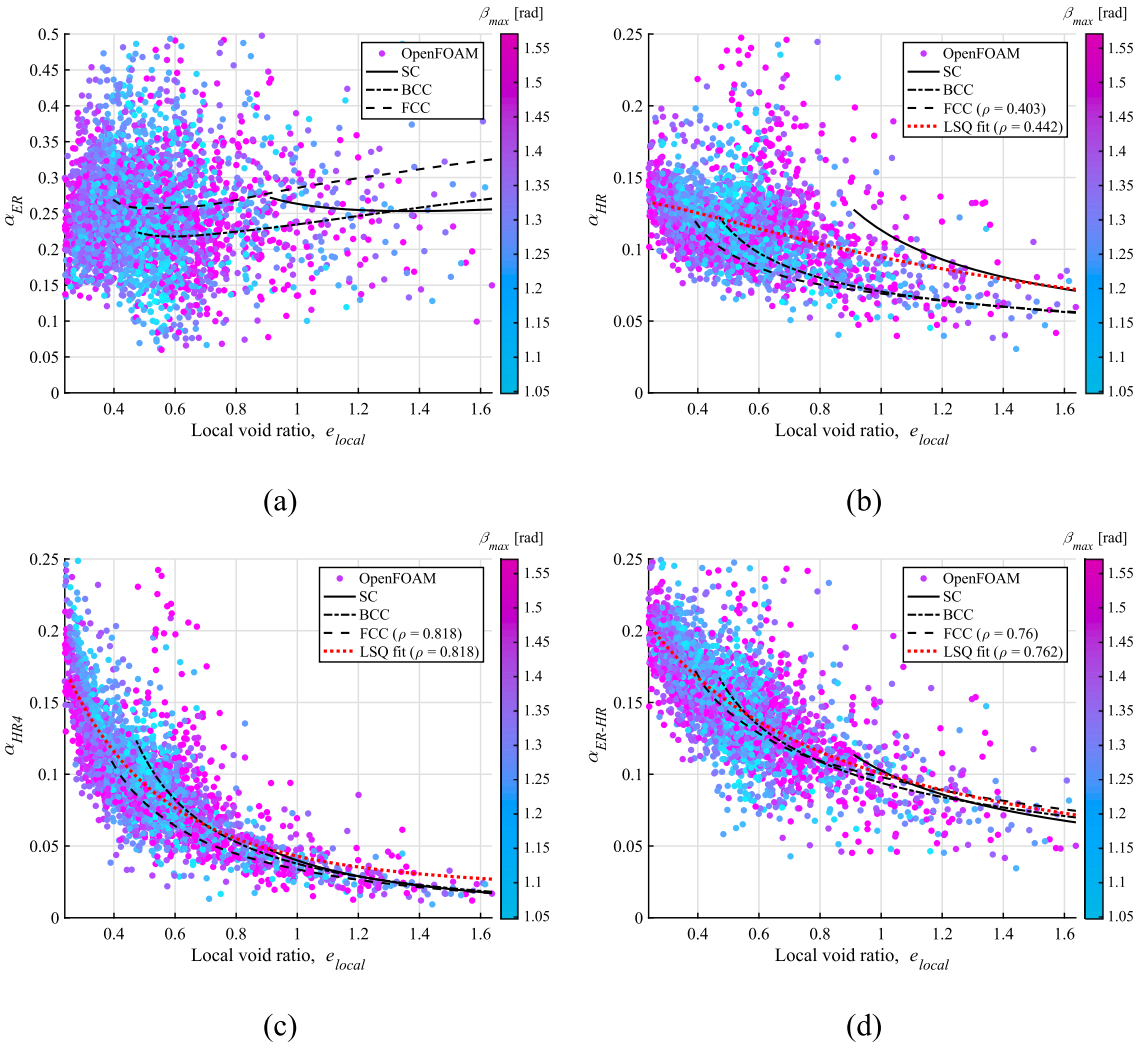

Fig. 17. Comparison of α versus e_{local} between an OF simulation and analytical models for $Cu = 2.00$ and $e = 0.468$. Marker colour gives the maximum angle of the throat face (β_{max}). (a) *ER* model. (b) *HR* model. (c) *HR*4 model. (d) *ER-HR* model.

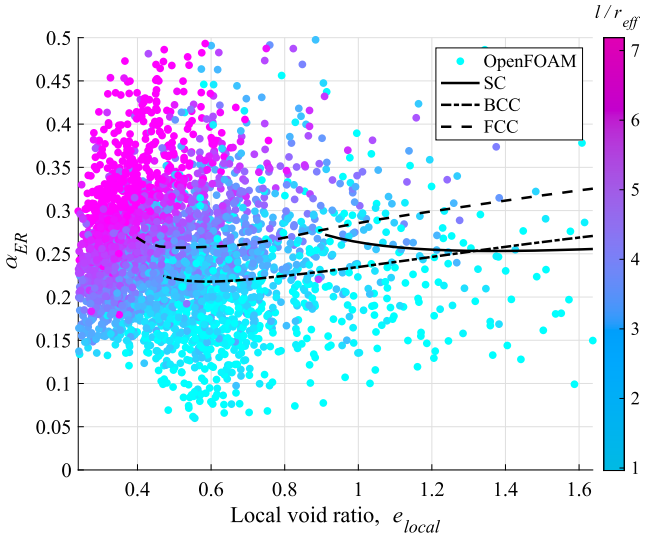

Fig. 18. Comparison of α versus e_{local} between an OF simulation and analytical models for $Cu = 2.00$ and $e = 0.468$. Marker colour gives the normalised throat length (l/r_{eff}).

face particles do not form a closed loop and the largest gap in the loop is orthogonal to the flow direction. For a dense packing ($e = 0.536$, Fig. 10 (b)), the VV method exhibited a good performance, with an obvious peak in the distribution of θ at $\theta = 0$. However, the CC method still does not effectively capture the flow direction.

A tabular summary of the analysis of the θ values for all the packings considered is provided in Table 1. θ_{peak} is defined as the θ value which has the most data points considering a histogram with 32 bins ($(n-1)\frac{\pi}{64} \leq \theta \leq n\frac{\pi}{64}$). The mean θ values (θ_{mean}), the standard deviations (SD θ) and the proportion of θ values with $\theta \leq \frac{\pi}{4}$ (denoted as $P_{\theta \leq \frac{\pi}{4}}$) are also shown. In all cases, the VV approach has a superior performance based on all the accuracy measures (θ_{peak}, θ_{mean}, and $P_{\theta \leq \frac{\pi}{4}}$) when compared with the CC approach. Where the VV approach is used, $P_{\theta \leq \frac{\pi}{4}}$ values of up to 75% are attained, however this decreases with reducing sample density (i.e. increasing void ratio). In general, while these data indicate that the denser samples are better suited to simulations using a PNM, with the VV method being the preferable approach, the results suggest that flow in a dilute system should not be simulated using a PNM. Based upon these analyses, hereinafter we only consider the VV approach and packed granular systems which are dense enough to transmit forces. To get an indication of the likely range of relevant void ratios we considered some prior studies: in their DEM simulations of isotropically compressed spheres, Shire and O'Sullivan, (2016) found that $0.558 < e < 0.714$ for $Cu = 1.2$ and $0.467 < e < 0.555$ for $Cu =$

Table 3
Tabular summary of ρ and R^2 values of analytical and the LSQ best-fit to the OF data for various models.

		ρ						R^2					
		HR		*HR4*		*ER-HR*		*HR*		*HR4*		*ER-HR*	
Cu	*e*	$\alpha(e)$	LSQ	$\alpha(e)$	LSQ	$\alpha(e)$	LSQ	$\alpha(e)$	LSQ	$\alpha(e)$	LSQ	$\alpha(e)$	LSQ
1.01	0.764	0.458	0.483	0.838	0.839	0.820	0.822	-0.225	0.233	0.529	0.704	0.604	0.675
	0.610	0.466	0.492	0.862	0.863	0.846	0.848	-0.395	0.242	0.501	0.744	0.631	0.718
	0.536	0.561	0.578	0.878	0.878	0.884	0.884	-0.738	0.335	0.296	0.772	0.449	0.781
1.2	0.764	0.403	0.489	0.759	0.769	0.797	0.803	-0.283	0.239	0.440	0.591	0.586	0.644
	0.613	0.371	0.444	0.815	0.818	0.817	0.820	-0.500	0.197	0.454	0.669	0.601	0.672
	0.555	0.481	0.520	0.849	0.849	0.853	0.854	-0.637	0.271	0.362	0.720	0.511	0.730
1.5	0.761	0.383	0.469	0.735	0.746	0.769	0.778	-0.185	0.220	0.459	0.556	0.579	0.605
	0.610	0.274	0.358	0.778	0.781	0.747	0.753	-0.400	0.128	0.484	0.610	0.539	0.567
	0.529	0.416	0.474	0.813	0.814	0.820	0.823	-0.476	0.225	0.437	0.662	0.585	0.678
2.0	0.751	0.403	0.472	0.762	0.769	0.735	0.741	-0.024	0.223	0.564	0.591	0.522	0.549
	0.603	0.346	0.403	0.800	0.801	0.728	0.733	-0.135	0.162	0.620	0.642	0.495	0.538
	0.468	0.403	0.442	0.818	0.818	0.760	0.762	-0.255	0.195	0.590	0.669	0.569	0.581

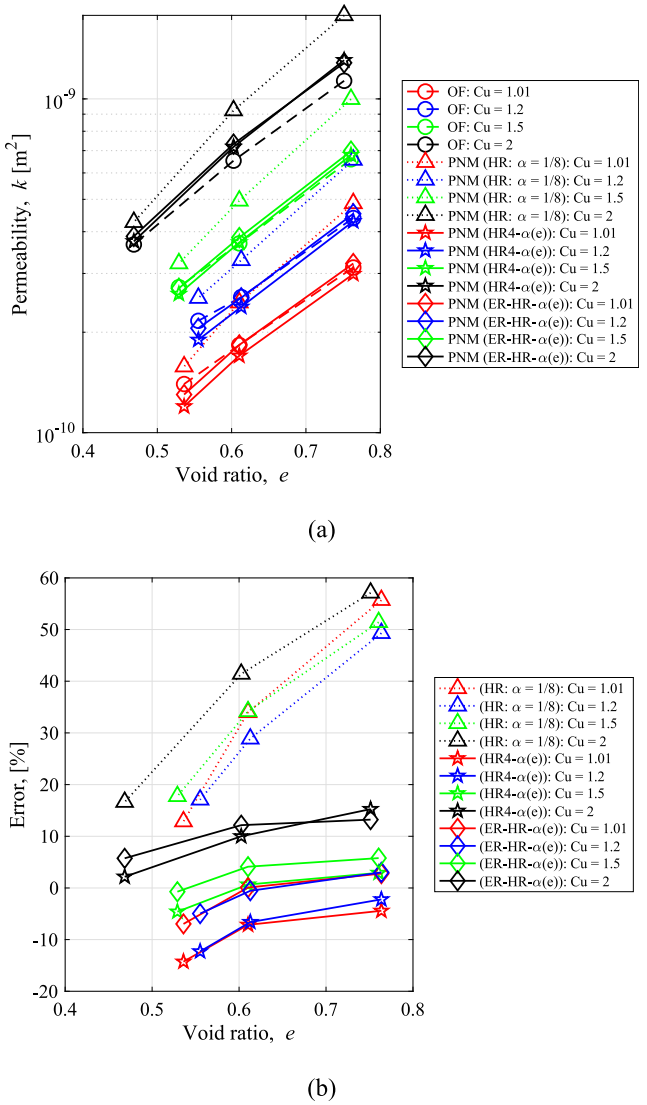

Fig. 19. Comparison of global permeabilities between an OF simulation and analytical models for random dense packings. (a) k versus e. (b) Relative error in the global permeabilities versus e.

2.0; for mono-dispersed spheres ($Cu \cong 1.0$), Song et al. (2008) stated that e_{max} is approximately 0.82 if an infinite friction coefficient is considered and e_{min} is approximately 0.58; for natural sands, higher e_{min} and e_{max} values are observed due to the rolling resistance that arises at contacts between non-spherical particles e.g. Nevada sand ($Cu = 1.8$; $e_{max} = 0.850$; $e_{min} = 0.570$), Ticino sand ($Cu = 1.5$; $e_{max} = 0.990$; $e_{min} = 0.574$) (Cho et al., 2006). Considering these studies, we restrict consideration to packings with $e < 0.80$ hereinafter.

Table 4
The permeability values (in $[m^2]$) of a variety of packings obtained from the OF and PNM simulations. The values in brackets are relative errors from the value obtained from the OF simulations.

Cu	*e*	OF	PNM HR:$\alpha = 1/8$	PNM HR4:$\alpha(e)$	PNM ER-HR:$\alpha(e)$
1.01	0.764	3.13×10^{-10}	4.87×10^{-10}	2.99×10^{-10}	3.21×10^{-10}
		(–)	(55.7%)	(-4.4%)	(2.8%)
	0.610	1.83×10^{-10}	2.45×10^{-10}	1.70×10^{-10}	1.83×10^{-10}
		(–)	(34.0%)	(-7.1%)	(0.1%)
	0.536	1.40×10^{-10}	1.58×10^{-10}	1.20×10^{-10}	1.30×10^{-10}
		(–)	(12.9%)	(-14.3%)	(-7.0%)
1.20	0.764	4.40×10^{-10}	6.56×10^{-10}	4.30×10^{-10}	4.53×10^{-10}
		(–)	(49.3%)	(-2.2%)	(3.0%)
	0.613	2.55×10^{-10}	3.29×10^{-10}	2.38×10^{-10}	2.54×10^{-10}
		(–)	(28.9%)	(-6.6%)	(-0.6%)
	0.555	2.16×10^{-10}	2.53×10^{-10}	1.90×10^{-10}	2.06×10^{-10}
		(–)	(17.1%)	(-12.3%)	(-5.0%)
1.50	0.761	6.59×10^{-10}	9.98×10^{-10}	6.79×10^{-10}	6.97×10^{-10}
		(–)	(51.4%)	(2.9%)	(5.8%)
	0.610	3.69×10^{-10}	4.95×10^{-10}	3.71×10^{-10}	3.84×10^{-10}
		(–)	(34.2%)	(0.7%)	(4.1%)
	0.529	2.73×10^{-10}	3.21×10^{-10}	2.60×10^{-10}	2.71×10^{-10}
		(–)	(17.7%)	(-4.6%)	(-0.7%)
2.00	0.751	1.13×10^{-9}	1.78×10^{-9}	1.31×10^{-9}	1.28×10^{-9}
		(–)	(57.1%)	(15.2%)	(13.2%)
	0.603	6.53×10^{-10}	9.23×10^{-10}	7.18×10^{-10}	7.32×10^{-10}
		(–)	(41.4%)	(10.0%)	(12.1%)
	0.468	3.66×10^{-10}	4.27×10^{-10}	3.74×10^{-10}	3.87×10^{-10}
		(–)	(16.6%)	(2.2%)	(5.7%)

Fig. 12(a) compares the local flow rates (Q_{local}) for each edge normalized by the global flow rate (Q_{global}) obtained from an OF simulation and a PNM simulation using the *HR* model for the assembly with $Cu = 1.01$ and $e = 0.536$. Each data point is coloured by the edge θ value. The ratio of the PNM data to the OF data tends to decrease as θ increases. Fig. 12(b) considers the same data as in Fig. 12(a) but a binary approach was used to isolate data points with $\theta \leq \frac{\pi}{4}$. Following Sufian et al. (2019), the correlation between the OF and PNM Q values was quantified using Pearson correlation coefficient values for all data and for data with $\theta \leq \frac{\pi}{4}$. With $\theta \leq \frac{\pi}{4}$, the correlation between normalized flow rate in PNM and OF was confirmed with a Pearson coefficient of 0.978. For all data, the Pearson coefficient decreased to 0.836; however, this is better than either of the models proposed by Sufian et al. (2019). The improvement in accuracy can be attributed to use of the VV approach instead of the CC

approach. In short, the PNM shows a good performance for flow when the θ value is close to zero and the proportion of edges with a θ which is close to zero is the key determinant of the validity of a PNM framework.

5.2. α values in mono-disperse packing

In Section 3, we developed an expression for α as a function of void ratio, e, using three types of regular packings. However, in random packings, the geometry of the throats is much more heterogeneous than in regular packings. Here we consider the applicability of the developed model to random packings. Exploiting the OF simulation data, "true" α values for each conductance model introduced in Section 2.2, except for the *FA* model, were back-calculated adopting the approach used in the analytical study described in Section 3.3. Only throats whose θ value is smaller than $\pi/4$ were considered in this section, so that we only considered the throats where a PNM approach can reasonably capture the flow direction, as there is limited value in assessing conductance models for local topologies that cannot be reasonably approximated by a pair of nodes connected by an edge.

Fig. 13 shows relationships between the α value obtained in OF and the local void ratio (e_{local}) for each throat in the specimen with $Cu = 1.01$ and $e = 0.764$ for the *ER*, *HR*, *HR*4, and *ER-HR* models. The α values calculated using the Zick and Homsy (1982) dataset for SC, BCC, and FCC packings are also plotted. Each data point is coloured based on the maximum angle of the throat face (β_{max}) (defined in Fig. 5) to assess the sensitivity to changes in the face geometry. There is a large scatter and no clear trend between α and e_{local} for the ER model (Fig. 13(a)); however, as shown in Fig. 13(b–d), for the *HR*, *HR*4, and *ER-HR* models, which all contain a r_h term, the α value back-calculated from the OF simulations decreases as e_{local} increases. These data do not support the constant α approach proposed in Chareyre et al. (2012) and agree with the observations made in the analytical study above (Fig. 6). In Fig. 13 (b-d), the results for the HR model (Fig. 13(b)) show a relatively large scatter. In effect, considering the colour of the data points, this scatter can be attributed to the oversimplification arising from using the A_f term to represent the face geometry as discussed in Section 3.3. On the other hand, the results for the *HR*4 and *ER-HR* models exhibit less scatter, which support using these models with $\alpha(e)$ models for random packings. A similar conclusion is drawn from the data for $Cu = 1.01$ and $e = 0.536$ shown in Fig. 14. For each of the *HR*, *HR*4, and *ER-HR* models, non-linear squares fitting (LSQ fit) was employed assuming that the optimal α value takes the following form:

$$\alpha^{LSQ}(e) = C_1\left(\frac{1}{1+e}\right)^3 + C_2\left(\frac{1}{1+e}\right)^2 + C_3\left(\frac{1}{1+e}\right) \tag{43}$$

and the best fit curves obtained are included in Fig. 13(b-d). The C_1, C_2, and C_3 obtained by Least Square curve fitting (Eq. (43)) to the OF data are presented in Table 2. The Pearson's correlation coefficients (ρ) obtained by comparing predictions by the analytical models (Eqs. (34) – (36)) or LSQ fit (Eq. (43)) and the OF data are also shown in the legends in Fig. 13(b-d). For the *HR*4 and *ER-HR* models, the overall trend of the analytical $\alpha(e)$ model and the LSQ curve agree well and there is a very small difference between the ρ values of the analytical model and LSQ fit. For the densest packing with $Cu = 1.01$ ($e = 0.536$), a similar result is obtained as shown in Fig. 14.

More detailed analysis to understand the poor performance of the *ER* model, was carried out using Fig. 15, where each marker for the *ER* model is coloured based on the normalized throat length defined as l/r_{eff} instead of β_{max}. The results show that the *ER* model is sensitive to the throat length. This length dependency arises because the throat cross-sectional area varies along the throat length so that if the length of the throat increases, the cross-sectional area at the end of the throat also increases.

5.3. α values in poly-disperse packings

The analyses of the lattice configurations could not consider the effects of polydispersity. To understand the influence of polydispersity on the proposed α model, the packings with $Cu = 2.00$, the most polydisperse cases considered in this study, were considered. The resulting data are presented in Fig. 16 for $e = 0.751$ and Fig. 17 for $e = 0.468$. For both cases, the prediction of α values made by the proposed $\alpha(e)$ expressions capture the general trend for *HR*4 and *ER-HR* models.

Fig. 18 is the same plot as Fig. 17(a) but each data point is coloured based on l/r_{eff}. The sensitivity of the *ER* model to changes in the length of the throat is again evident.

A tabular summary of the ρ and R^2 values for both the analytical model (Eqs. (34) – (36)) and the LSQ best-fit equation is provided in Table 3. For the range of *Cu* and *e* values considered here, the very small differences in the Pearson correlation coefficient (ρ) for *HR*4 and *ER-HR* models between $\alpha(e)$ and $\alpha^{LSQ}(e)$ show that the $\alpha(e)$ expressions capture the overall trend very well. Comparison of the R^2 values, however, shows that the $\alpha(e)$ expression gives some relatively large errors. The errors are smaller for the *ER-HR* model when $Cu = 1.01$, 1.2, 1.5, while the *HR*4 model gave better R^2 values for $Cu = 2$. Overall, the proposed *HR*4 and *ER* −*HR* models with the $\alpha(e)$ model can obtain results whose accuracy is comparable with the predictions using the LSQ best-fit to the OF data.

5.4. Global permeability prediction using developed models

The $\alpha(e)$ expression proposed as Eqs. (35) and (36) was implemented in a PNM and a simulation to obtain global permeability was conducted for each packing with a variety of *Cu* and *e* values and for each of selected models following the procedure outlined in 4.2. The *HR* model proposed by Chareyre et al. (2012) with a constant α value of $1/8$ and the *HR*4 and *ER-HR* models with $\alpha(e)$ were considered for the comparison.

Fig. 19(a) compares the global permeability values obtained by OF simulations and PNM simulations with three different models. The permeability values in Fig. 19(a) are summarised in Table 4. The *HR*4-$\alpha(e)$ and *ER-HR*-$\alpha(e)$ models capture the variation in permeability very well while the *HR* model with $\alpha = 1/8$ noticeably overpredicts the global permeability. The relative error in the global permeabilities is plotted in Fig. 19(b). For both the *HR*4-$\alpha(e)$ and *ER-HR*-$\alpha(e)$ expressions the error is within +/-15.2% for a wide range of *Cu* and *e*. This result is significant because the $\alpha(e)$ model is developed without any input from OF data and the result also supports a wide applicability of $\alpha(e)$ model without any calibration. Overall, no significant difference between the performances of the *HR*4-$\alpha(e)$ and *ER-HR*-$\alpha(e)$ expressions was observed, though it should be pointed out that the *HR*4 −$\alpha(e)$ model is computationally cheaper than the *ER-HR*-$\alpha(e)$ model as the latter requires the calculation of the inscribed circle radius.

6. Conclusions

The overall aim of this study was to develop an accurate and efficient coupled CFD-DEM modelling framework that can capture local heterogeneities in the fluid flow. Use of a PNM to simulate fluid flow overcomes many of the limitations associated with other options for CFD-DEM. However the accuracy of a PNM model depends on the accuracy of the local conductance model used. This study has critically assessed existing model for local conductance and proposed a new formulation. The analyses drew on data presented in Zick and Homsy (1982), as well as a new data set of rigorously validated fully-resolved CFD data generated using OpenFOAM. The samples comprised random packings of spheres with linear PSDs. This study can be seen as complementary to the recent work of Rong et al. (2020), who also analysed local conductances using fully resolved flow simulations. While the data provided by

Rong et al. indicate their method is accurate, the method proposed in the current study has the advantage of not requiring additional numerical simulations of flow through individual pore throats.

The main findings are as follows:

1. The choice of the throat radius R and the shape factor α, which represent the throat geometry, is critical for modelling the local conductance, formulated as $\alpha\pi R^4/L$ following the Hagen-Poiseuille equation. For expressions that use r_h, our data has shown that the α value should reduce as the local void ratio increases. Using this new insight we proposed new expressions for α as that consider the local void ratio (e) that can be implemented in four different conductance models. Use of these new expressions will give improvements in accuracy in comparison with the constant α value proposed in Chareyre et al. (2012). OpenFOAM simulation data were used to confirm the applicability of these expressions to random assemblies of spheres by considering both back calculated α values and comparing values for global permeability.
2. Analyses of flow in the void space for regular packings of uniform spheres revealed limitations in the existing local conductance expressions. Expressions based on A_f are sensitive to changes in the pore throat topology. Using r_{eff} instead of A_f improves the robustness of these expressions.
3. Using the Voronoi vertices as the PNM nodes to flow directions improves the ability of a PNM to accurately capture local flow. The PNM framework is not well suited to simulate flow in dilute packings because the true local flow direction and the local flow direction predicted by the PNM differ significantly.

CRediT authorship contribution statement

Tokio Morimoto: Conceptualization, Methodology, Software, Validation, Formal analysis, Investigation, Data curation, Writing – original draft. **Budi Zhao:** Methodology, Writing – review & editing. **David M.G. Taborda:** Writing – review & editing, Supervision, Funding acquisition. **Catherine O'Sullivan:** Writing – review & editing, Supervision, Funding acquisition.

Declaration of Competing Interest

The authors declare that they have no known competing financial interests or personal relationships that could have appeared to influence the work reported in this paper.

Acknowledgements

The numerical work of Dr. Budi Zhao was funded via EPSRC grant EP/P010393/1. Mr. Tokio Morimoto was funded by the European Union's Horizon 2020 research and innovation program Marie Skłodowska-Curie grant agreement MATHEGRAM No. 813202. OpenFOAM simulations were conducted on the Research Computing Service facilities at Imperial College London (DOI: 10.14469/hpc/2232).

Appendix A. Validation of the fully-resolved CFD method

The MSP-OpenFOAM framework was validated by considering FCC packings of uniform spheres and by comparing the results in terms of drag coefficient (c_d) values with data from the study by Zick and Homsy (1982). This approach to the validation of the CFD technique in terms of c_d follows those adopted in previous studies (e.g., Knight et al., 2020, Zhao and O'Sullivan, 2022). The validation confirms that the adopted approach can correctly capture permeability and fluid-particle interactions given an adequate resolution of discretization.

In the OF simulations of the FCC packing, 5 layers of 2 particles were considered as shown in Fig. A1(a). If the distance between the particle centroids is d, the diameter of the particles, D, was varied from $0.8d$ to d, to give $0.350 < e < 1.637$, where e is the void ratio. The positions and diameters of the particles were input to MSP. The ratio of D to the mesh length (ds_c), which is illustrated in Fig. A1(b), was varied from 20 to 50 to examine the effect of element size on the data generated. The drag force on the central particle (indicated by a black arrow in Fig. A1(a)) was exported

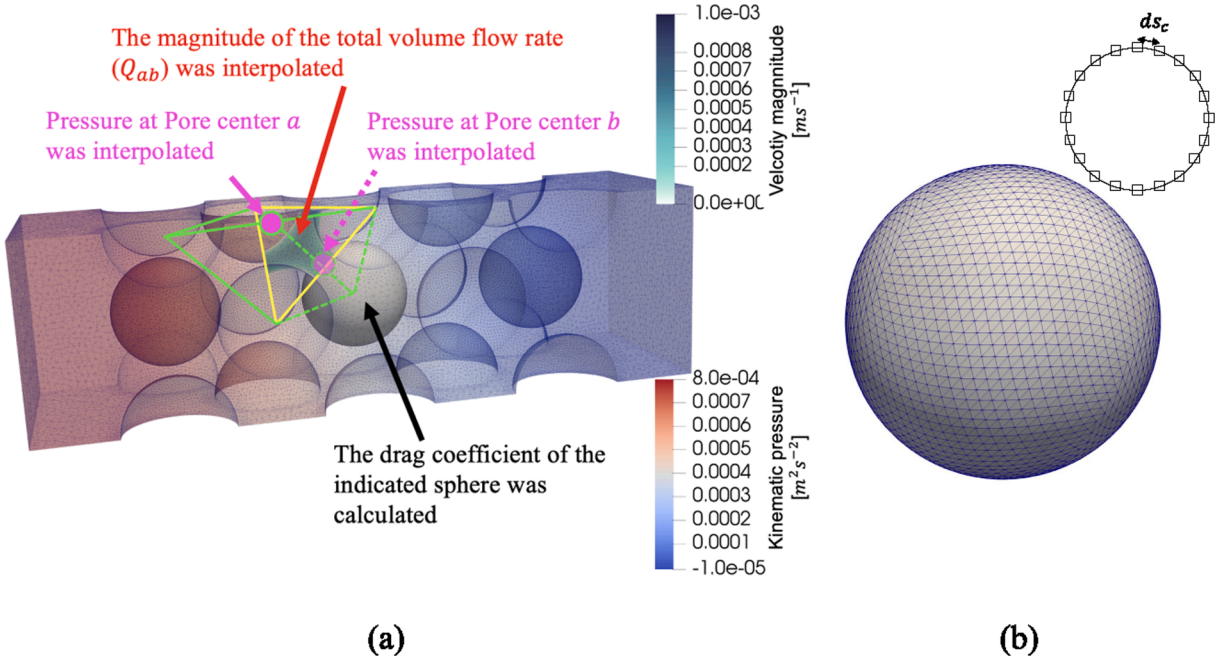

Fig. A1. Schematic illustration of OF simulations using FCC packings for validation. (a) The geometry of an FCC model and the pressure distribution (b) Mesh seeds on a sphere surface ($\frac{D}{ds_c} = 30$) and the definition ofds_c

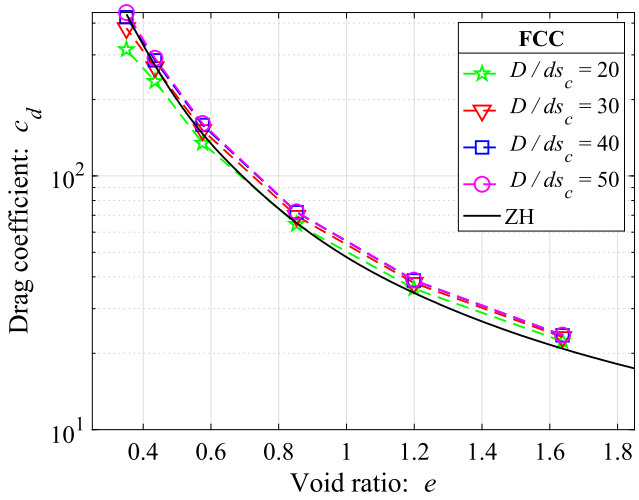

Fig. A2. Validation of OF study results in terms of c_d versus e using FCC packings.

from OpenFOAM and the c_d value was calculated using Eq. (16). The OF simulation results are compared with the Zick and Homsy data in Fig. A2. With $\frac{D}{ds_c} = 20$, the OF simulation underestimated c_d for the denser packings, however for $\frac{D}{ds_c} = 30$, the error is $\leq 12\%$ for a wide range of void ratios ($0.350 < e < 1.637$). Following Eq. (15), accurately predicting c_d is equivalent to accurately predicting the permeability. The relative error is relatively small considering the large range of void ratio values and similar to the error level documented in previous studies (e.g. Knight et al., 2020). Thus $\frac{D}{ds_c} = 30$ was also used for the detailed analyses presented here. Note that the conductance models developed in this study based on the analytical data by Zick and Homsy (1982) and therefore do not depend on the mesh quality of the OF simulations.

Appendix B. Verification of analytically determined Γ value

The analytical approach to the determination of Γ values employed in Section 3.2 requires some assumptions: (a) the pressure gradient is constant through the packing; and (b) the flow direction at the throat face is normal to the throat face. Therefore, the derived Γ values need independent verification. The analytical Γ values determined by analysing the Zick and Homsy (1982) data were verified using the OF simulation results for the FCC packings introduced above. The Γ value of the throat indicated in Fig. A1(a) was calculated following the post-process procedure outlined in Section 4.2.

A comparison between values calculated from OF results for regular packings, Γ_{ab}^{RP}, and those obtained from Eq. (30) is shown in Table B1. For a wide range of e values ($0.35 < e < 1.64$), a good agreement was obtained, which confirms the viability of using the Zick and Homsey data to estimate Γ_{ab}^{RP}.

Table B1
Tabular summary of comparison between Γ_{ab}^{RP} values of OpenFOAM and analytical studies for FCC packings.

D	e	OpenFOAM Γ_{ab}^{RP} $[m^4]$	Analytical Γ_{ab}^{RP} $[m^4]$
$0.8d$	1.64	3.152×10^{-14}	3.095×10^{-14}
$0.9d$	0.85	8.617×10^{-15}	8.828×10^{-15}
d (densest)	0.35	1.367×10^{-15}	1.202×10^{-15}

Appendix C. Consideration of periodic boundaries in a pore network model

This study considers periodic boundaries for the x- and y-directions to minimise boundary effects. Here, referring to Fig. C1, we briefly explain how the periodic boundaries were implemented for completeness.

(1) A "cut-off distance" is specified and the particles whose distance from one side of a periodic boundary is smaller than the cut-off distance are copied to the corresponding position just outside the opposite periodic boundary. This procedure is conducted $3^n - 1$ times, where n is the number of periodic boundaries considered in the simulation. The original domain is called the "local" domain and the other domains created by this procedure are called as "ghost" domains. There are $3^n - 1$ ghost domains in the PNM simulation. Particles, whose centres are in the local domain, are "local" particles and the that are copied and mapped are "ghost" particles. There are two ID systems for the particles: (1) the local ID system, where a ghost particle has a different ID from the original particle, and (2) the global ID system, where ghost particles have the same IDs as the original particles. Local particles have the same local ID and global ID. When a new particle is created, we assign a new local ID to the particle and the ID of the original particle is also stored as the global ID.

(2) The local IDs, positions, and radii of the local and ghost particles are passed to TetGen and the weighted Delaunay triangulation is conducted. TetGen returns the local IDs of particles which define each pore and connectivity information between pores.

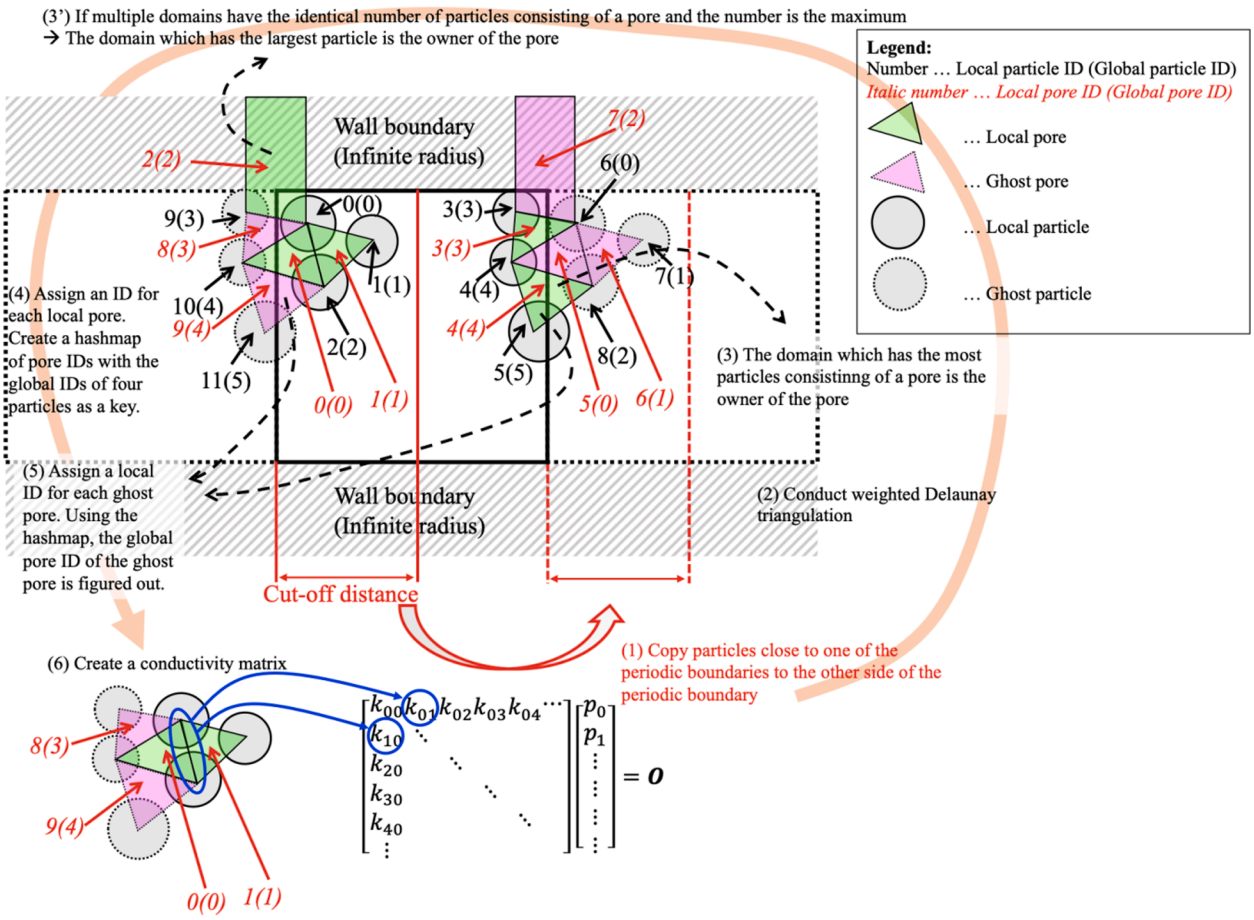

Fig. C1. Schematic illustration of the procedure to consider periodic boundaries in a PNM simulation.

(3) The "local" and "ghost" pores are defined following Beyer et al. (2005). For each pore, we check whether the particles defining the pore are local or ghost particles. If all the particles are local, the pore is a local pore. When a mixture of local and ghost particles define a pore, the pore is assigned to whichever the domain assigned to the largest particle. There is a system of local and global IDs for the pores.

(4) Once local and ghost pores are determined, we assign identical local and global IDs to the local pores starting from zero. Once we finish giving the IDs to the local pores, we create a hashmap which stores the global pore ID of each local pore with the global particle IDs consisting of the local pore being the key.

(5) After creating the hashmap, each ghost pore is assigned for a new local pore ID, and the global ID of the original pore is assigned to the ghost pore, with the original pore being detected using the global particle IDs of the particles consisting of the ghost pore. There are two possibilities of the original local pore of a ghost pore not being found. One occurs when the cut-off distance is too small and can be resolved by increasing the cut-off distance. The other is due to the occurance of a lattice-like particle configuration (which can occur in regular packings), where the weighted Delaunay triangulation is not unique. In this case, a very small perturbation in the particle positions can resolve the problem.

(6) Each local pore is checked and for each pore connection the local pore has, the Γ value is calculated, and the elements of the conductivity matrix is filled using the global pore IDs of the local pore and adjacent pore.

References

Ahrens, J., Geveci, B., Law, C., 2005. ParaView: An End-User Tool for Large Data Visualization, Visualization Handbook. Elsevier. ISBN-13: 978-0123875822.

Balay, S., Gropp, W.D., McInnes, L.C., Smith, B.F., 1997. Efficient management of parallelism in object-oriented numerical software libraries. In: Arge, E., Bruaset, A. M., Langtangen, H.P. (Eds.), Modern Software Tools for Scientific Computing. Birkhäuser Boston, Boston, MA, pp. 163–202. https://doi.org/10.1007/978-1-4612-1986-6_8.

Balay, S. et al., 2021. PETSc Users Manual. Argonne National Laboratory.

Beyer, T., Schaller, G., Deutsch, A., Meyer-Hermann, M., 2005. Parallel dynamic and kinetic regular triangulation in three dimensions. Comput. Phys. Commun. 172 (2), 86–108.

Bryant, S., Blunt, M., 1992. Prediction of relative permeability in simple porous media. Phys. Rev. A 46 (4), 2004–2011. https://doi.org/10.1103/PhysRevA.46.2004.

Catalano, E., Chareyre, B., Barthélémy, E., 2014. Pore-scale modeling of fluid-particles interaction and emerging poromechanical effects. Int. J. Numer. Anal. Meth. Geomech. 38 (1), 51–71.

Chareyre, B., Cortis, A., Catalano, E., Barthélemy, E., 2012. Pore-scale modeling of viscous flow and induced forces in dense sphere packings. Transp. Porous Media 94 (2), 595–615. https://doi.org/10.1007/s11242-012-0057-2.

Che, H., O'Sullivan, C., Sufian, A., Smith, E.R., 2021. A novel CFD-DEM coarse-graining method based on the Voronoi tessellation. Powder Technol. 384, 479–493. https://doi.org/10.1016/j.powtec.2021.02.025.

Cho, G., Dodds, J., Santamarina, J.C., 2006. Particle shape effects on packing density, stiffness and strength: natural and crushed sands. J. Geotech. Geoenviron. Eng. 132 (5), 591–602. https://doi.org/10.1061/(ASCE)1090-0241(2006)132:5(591).

Cundall, P.A., Strack, O.D.L., 1979. A discrete numerical model for granular assemblies. Géotechnique 29 (1), 47–65. https://doi.org/10.1680/geot.1979.29.1.47.

Di Felice, R.D., 1994. The voidage function for fluid-particle interaction systems. Int. J. Multiphase Flow 20 (1), 153–159. https://doi.org/10.1016/0301-9322(94)90011-6.

El Shamy, U., Zeghal, M., 2007. A micro-mechanical investigation of the dynamic response and liquefaction of saturated granular soils. Soil Dyn. Earthq. Eng. 27 (8), 712–729. https://doi.org/10.1016/j.soildyn.2006.12.010.

El Shamy, U., De Leon, O., Wells, R., 2013. Discrete element method study on effect of shear-induced anisotropy on thermal conductivity of granular soils. Int. J. Geomech. 13 (1), 57–64. https://doi.org/10.1061/(ASCE)GM.1943-5622.0000165.

Ergun, S., 1952. Fluid flow through packed columns. Chem. Eng. Prog. 48, 89–94.
Feng, Y.T., Han, K., Owen, D.R.J., 2007. Coupled lattice Boltzmann method and discrete element modelling of particle transport in turbulent fluid flows: Computational issues. Int. J. Numer. Meth. Eng. 72 (9), 1111–1134. https://doi.org/10.1002/nme.2114.
Knight, C., 2019. Fluid flow and drag in polydisperse granular materials subject to laminar seepage flow. Ph.D. thesis, Imperial College London, London, UK. https://doi.org/10.25560/67823.
Knight, C., 2021. mesh-sphere-packing. https://github.com/chrisk314/mesh-sphere-packing.
Knight, C., O'Sullivan, C., van Wachem, B., Dini, D., 2020. Computing drag and interactions between fluid and polydisperse particles in saturated granular materials. Comput. Geotech. 117, 103210. https://doi.org/10.1016/j.compgeo.2019.103210.
Kress, J., Yun, T.S., Narsilio, G.A., Evans, T.M., Lee, D.S., 2012. Evaluation of hydraulic conductivity in 3D random and heterogeneous particulate materials using network model. Comput. Geotech. 40, 45–52. https://doi.org/10.1016/j.compgeo.2011.09.007.
Mason, G., Morrow, N.R., 1991. Capillary behavior of a perfectly wetting liquid in irregular triangular tubes. J. Colloid Interface Sci. 141 (1), 262–274. https://doi.org/10.1016/0021-9797(91)90321-X.
Patzek, T.W., Silin, D.B., 2001. Shape factor and hydraulic conductance in noncircular capillaries: I. One-phase creeping flow. J. Colloid Interface Sci. 236 (2), 295–304. https://doi.org/10.1006/jcis.2000.7413.
Rong, L.W., Dong, K.J., Yu, A.B., 2020. Lattice-Boltzmann computation of hydraulic pore-to-pore conductance in packed beds of uniform spheres. Chem. Eng. Sci. 224, 115798. https://doi.org/10.1016/j.ces.2020.115798.
Sholokhova, Y., Kim, D., Lindquist, W.B., 2009. Network flow modeling via lattice-Boltzmann based channel conductance. Adv. Wat. Res. 32 (2), 205–212.
Shire, T., O'Sullivan, C., 2016. Constriction size distributions of granular filters: a numerical study. Géotechnique 66 (10), 826–839. https://doi.org/10.1680/jgeot.15.P.215.
Si, H., 2015. TetGen, a Delaunay-based quality tetrahedral mesh generator. ACM Trans. Math. Software (TOMS) 41 (2), 1–36. https://doi.org/10.1145/2629697.
Šmilauer, V. et al., 2015. Yade documentation 2nd ed. the yade project.
Song, C., Wang, P., Makse, H.A., 2008. A phase diagram for jammed matter. Nature 453 (7195), 629–632. https://doi.org/10.1038/nature06981.
Sufian, A., Knight, C., O'Sullivan, C., van Wachem, B., Dini, D., 2019. Ability of a pore network model to predict fluid flow and drag in saturated granular materials. Comput. Geotech. 110, 344–366. https://doi.org/10.1016/j.compgeo.2019.02.007.
Sweijen, T., Hassanizadeh, S.M., Chareyre, B., Zhuang, L., 2018. Dynamic pore-scale model of drainage in granular porous media: the pore-unit assembly method. Water Resour. Res. 54 (6), 4193–4213. https://doi.org/10.1029/2017WR021769.
Thompson, K.E., Fogler, H.S., 1997. Modeling flow in disordered packed beds from pore-scale fluid mechanics. AIChE J. 43 (6), 1377–1389.
Tsuji, Y., Kawaguchi, T., Tanaka, T., 1993. Discrete particle simulation of two-dimensional fluidized bed. Powder Technol. 77 (1), 79–87. https://doi.org/10.1016/0032-5910(93)85010-7.
Uhlmann, M., 2005. An immersed boundary method with direct forcing for the simulation of particulate flows. J. Comput. Phys. 209 (2), 448–476.
van der Linden, J.H., Sufian, A., Narsilio, G.A., Russell, A.R., Tordesillas, A., 2018. A computational geometry approach to pore network construction for granular packings. Comput. Geosci. 112, 133–143. https://doi.org/10.1016/j.cageo.2017.12.004.
Van Oosterom, A., Strackee, J., 1983. The solid angle of a plane triangle. IEEE Trans. Biomed. Eng. 2, 125–126. https://doi.org/10.1109/TBME.1983.325207.
Weller, H.G., Tabor, G., Jasak, H., Fureby, C., 1998. A tensorial approach to computational continuum mechanics using object-oriented techniques. Comput. Phys. 12 (6), 620–631. https://doi.org/10.1063/1.168744.
Wu, Y., Hou, Q., Yu, A., 2019. Pore-scale study of fluid flow and drag force in randomly packed beds of different porosities. Ind. Eng. Chem. Res. 58 (12), 5041–5053.
Wu, Y., Hou, Q., Qi, Z., Yu, A., 2021. Particle–pore scale modelling of particle–fluid flows. Chem. Eng. Sci. 235, 116500. https://doi.org/10.1016/j.ces.2021.116500.
Xu, B.H., Yu, A.B., 1997. Numerical simulation of the gas-solid flow in a fluidized bed by combining discrete particle method with computational fluid dynamics. Chem. Eng. Sci. 52 (16), 2785–2809.
Zhao, B., O'Sullivan, C., 2022. Fluid particle interaction in packings of monodisperse angular particles. Powder Technol. 395, 133–148.
Zhou, Z.Y., Kuang, S.B., Chu, K.W., Yu, A.B., 2010. Discrete particle simulation of particle–fluid flow: model formulations and their applicability. J. Fluid Mech. 661, 482–510.
Zhu, H.P., Zhou, Z.Y., Yang, R.Y., Yu, A.B., 2008. Discrete particle simulation of particulate systems: a review of major applications and findings. Chem. Eng. Sci. 63 (23), 5728–5770.
Zick, A.A., Homsy, G.M., 1982. Stokes flow through periodic arrays of spheres. J. Fluid Mech. 115, 13–26. https://doi.org/10.1017/S0022112082000627.